RESEARCH ARTICLE

Extreme temperature events monitored by Raman lidar: Consistency and complementarity with spaceborne observations and modelling

Alexandre Baron 🄍 | Patrick Chazette 🄍 | Julien Totems 🄍

Laboratoire des Sciences du Climat et de L'environnement, Université Paris-Saclay, CNRS, CEA, UVSQ, Gif-sur-Yvette, France

Correspondence
Alexandre Baron, Laboratoire des Sciences du Climat et de L'environnement, Université Paris-Saclay, CNRS, CEA, UVSQ, 91191, Gif-sur-Yvette, France.
Email: alexandre.baron@univ-reunion.fr

Present address
Alexandre Baron, Laboratoire de l'Atmosphère et des Cyclones (LACy), UMR 8105, Université de la Réunion – CNRS – Météo-France, Saint-Denis, France

Abstract

Two extreme temperature events (ETEs), both triggered by atmospheric blocking situations, were monitored by a pure rotational Raman lidar 20 km south of Paris. The first ETE lasted 6 days in late February 2018 with the onset of a cold wave surging from Siberia, and the second was a short heatwave that occurred at the end of July 2020. After calibration using simultaneous radiosoundings, lidar vertical profiles of temperature are derived with an uncertainty of less than 1 °C within both the planetary boundary layer and the lower/middle free troposphere (~3/6 km above ground level [a.g.l.] for day/night), with a final vertical resolution of 50 m and a temporal resolution of 30 min. Such capabilities fulfil the observational requirements of the World Meteorological Organisation and contribute to fill a gap left behind by current operational instruments, which struggle to follow the diurnal cycle of the planetary boundary layer due to insufficient spatial and temporal resolutions in the low troposphere. These case studies allow to assess how such weather events are represented by numerical weather prediction modelling and whether they can be correctly observed by the Infrared Atmospheric Sounding Interferometer (IASI) spaceborne mission. Our results demonstrate that during these events both ECMWF reanalyses and forecasts are in overall very good accordance with lidar observations (correlation >0.9 in average). Still, they show warm biases (~1°C–2°C) compared with the lidar and improvable temperature field representation in the boundary layer. The radiances measured by IASI, assimilated in the operational model, do not capture temperature profiles adequately below ~2–3 km a.g.l., mainly due to the altitude location of its weighting functions. The bias computed against the lidar reaches 2°C during the heatwave and 4°C during the cold wave case in the first 2 km of the atmosphere, beyond expected errors found in the literature.

KEYWORDS
comparison, ERA5, IASI, IFS, observational requirements, rotational Raman

1 | INTRODUCTION

Anthropic activity-induced climate change calls for adaptation strategies within human societies. Among these needs, the demand in reliable weather forecasting of extreme events is strong (e.g., Linnenluecke et al., 2012). Indeed, extreme meteorological conditions induce a substantial stress on populations (Deschênes & Moretti, 2009), on fauna and flora (Parmesan et al., 2000; Rosenzweig et al., 2001) and can result in heavy costs (Frame et al., 2020). While a weather event can be extreme in terms of wind or precipitation, the study presented here will be focused on extreme events of temperature (ETEs). An ETE can be defined in several ways, examples are given in the study by Domonkos and Piotrowicz (1998). Here we followed the protocol used by the French meteorological services, Météo-France (see Appendix A). In the context of rising temperatures, it is essential to forecast and follow the evolution of cold and heat waves using both well-resolved vertical measurement networks and weather modelling. Unlike water vapour, temperature is among the best observed and modelled meteorological variables. It is a key variable as it controls the atmospheric stability and is implicated in the energy balance of the atmosphere. Monitoring atmospheric temperature with the highest accuracy is of crucial importance when computing relative humidity for the formation or evaporation of clouds, especially in models where these mechanisms are associated with threshold effects. This monitoring is currently performed by a set of operational tools such as ground-based meteorological stations, a network of synchronized radiosounding facilities and space platforms dedicated to earth observations such as the MetOp (Meteorological Operational) A and B satellites with the Infrared Atmospheric Sounding Interferometer (IASI, Clerbaux et al., 2009) or the Aqua mission carrying the Atmospheric Infrared Sounder (AIRS, e.g., Aumann et al., 2003). The Global Navigation Satellite System–Radio Occultation (GNSS-RO) technique (Kursinski et al., 1997) is also to be noted in the landscape of observational data sets to be assimilated into numerical weather prediction (NWP) models such as the Integrated Forecasting System (IFS). Although these observational means reach an impressive accuracy, there are some gaps that can be identified. In terms of temporal resolution, radiosondes are spaced 12 h apart and cannot accurately capture intra-day variations, the launches are globally distributed, but the southern hemisphere and the poles suffer from a smaller number of stations. Ground-based weather stations have a good spatial and temporal coverage over the continents and are enriched with measurements from sea buoys or along sea routes. On their side, spaceborne observations offer a global coverage of the Earth, a temporal resolution depending on the return time of the satellite (e.g., twice a day for polar-orbiting

platforms such as the MetOp series) but a weak vertical resolution inherent to passive sensors (Wulfmeyer et al., 2005). Ultimately, the most concerning gap not already filled by these existing operational measurements is the monitoring at high temporal and vertical resolutions of the first kilometres of atmosphere (typically 3 km) and their diurnal cycle. This motivated the World Meteorological Organisation (WMO, 2017) to establish observational requirements and goals for each application area of climate and meteorological prediction (e.g., very short range forecasting, high-resolution NWP). To complete the set of observations relying heavily on in situ and passive remote sensing measurements, active remote sensing techniques are excellent candidates to reach high vertical and temporal resolutions.

The lidar technique, although restricted to a single location when ground-based, allows continuous measurements of the low troposphere at high spatiotemporal resolution. Temperature measurements using lidar constitute promising candidates for breakthrough WMO requirements. They can be performed in the upper atmosphere simply by using the integration technique on the elastic backscatter signal, where only molecular scattering occurs (Hauchecorne & Chanin, 1980). As the latter technique suffers from the presence of aerosol in the low/middle troposphere, the method privileged nowadays to retrieve the tropospheric temperature relies on the rotational Raman (RR) scattering of the most abundant atmospheric molecules. RR lidar, first proposed by Cooney (1972)), uses the temperature dependence of the RR spectra of dioxygen (O_2) and dinitrogen (N_2). Since then, remarkable works have been conducted following technological advances to improve RR lidar systems capabilities and obtain a pure RR (PRR) backscatter clear from elastic scattering contamination (Arshinov et al., 1983; Nedeljkovic et al., 1993; Penney et al., 1974; Vaughan et al., 1993). Among notable advances, the design of interference filters (Hammann & Behrendt, 2015) is instrumental for the PRR technique. The filters fineness is critical both to sufficiently reject the laser wavelength, thus preventing signal contamination by elastic scattering (Di Girolamo et al., 2004; Mattis et al., 2002) and to perform temperature measurements in daylight (Arshinov et al., 2005; Radlach et al., 2008).

Noteworthy state-of-the-art PRR lidars are described in the literature. In Switzerland, Balin et al. (2004) present the observations from a PRR lidar at the Jungfraujoch alpine station, with which measurements of relative humidity have been achieved by combining PRR measurements of temperature with simultaneous water vapour mixing ratio measurements from a vibrational Raman channel. Nowadays, the Raman Lidar for Meteorological Observation (RALMO) at the Payerne EARLINET station is capable of providing continuous measurements of

meteorological variables (Dinoev et al., 2013; Martucci et al., 2021) and allows joint studies of the coupled cycles of aerosols and water vapour (Navas-Guzmán et al., 2019). In Germany, PRR lidars have been developed since the beginning of the 2000s (Behrendt et al., 2004; Behrendt & Reichardt, 2000), with a focus on meteorological and turbulent processes. Aiming to describe mechanisms inherent to the planetary boundary layer (PBL) dynamics, the high temporal resolution and low altitude temperature measurements (Hammann et al., 2015) of these lidars were used to investigate the moments of turbulent temperature fluctuations (Behrendt et al., 2015), or the strength of the inversion layer (Lange et al., 2019). The assimilation of lidar-derived temperature profiles in WRF is also to be noted (Adam et al., 2016). In Italy, the BASIL lidar (Di Girolamo et al., 2017) has prominently been applied to meteorological monitoring within the framework of the Hydrological cycle in the Mediterranean eXperiment (HyMeX), especially to water vapour mixing ratio and/or temperature inter-comparisons (Di Girolamo et al., 2020; Summa et al., 2018).

Benefiting from these studies, a PRR channel operating in the UV has been developed to equip the former Water vapour and Aerosol LIdar (Chazette et al., 2014), renamed Weather and Aerosol LIdar (WALI). As discussed by Di Girolamo et al. (2004)), the use of the 355 nm wavelength makes the system less sensitive to the visible sky background during daytime measurements while being also eye-safe a few metres away from the laser emission. The WALI stands out from the pre-existing PRR lidars by positioning itself as a versatile tool, compact and easily transportable on-board the Mobile Atmospheric Station (Totems & Chazette, 2016). It can perform continuous measurements autonomously with low power consumption (<1 kW) and reliable stability. Currently devoted to aerosol and meteorological measurements during instrumental field campaigns (Chazette, Totems, et al., 2016; Totems et al., 2019), this lidar architecture could be employed for autonomous ground-based meteorological lidar stations (Flamant et al., 2021).

The present study aims to present the potential of PRR lidar to follow at high resolutions the rapid temperature variations of the lower atmosphere, typically the first 3 km, as they occur during the extreme temperature events (ETEs). This way, we expect to fill observation gaps of actual operational instruments. This is achieved through comparisons between temperature retrievals from passive spaceborne measurements, modelling and WALI measurements recorded during two periods of ETEs over Saclay (~20 km south of Paris, France). The first sequence of measurements has been performed during 6 days, from 21 to 27 February 2018, and was marked by the onset of a cold wave (CW). The second sequence lasted height days, from 26 July to 02 August 2020, and recorded the emergence of the first 2020 heat wave (HW) felt in Europe. These datasets contain intense temporal and vertical temperature gradients. They present an opportunity to compare PRR lidar temperature to the level 2 products of IASI (Schlüssel et al., 2005) and to check the coherence of operational modelling with the lidar measurements. Hence, we consider products of the European Centre for Medium-Range Weather Forecasts (ECMWF) IFS forecast outputs. We also study the improvement in terms of temperature following the reanalysis process via the ERA5 reanalysis product (Hersbach et al., 2020), as previously performed for atmospheric water vapour (Chazette, Flamant, et al., 2016).

The paper is structured as follows. Section 2 first presents the tools used in the study, namely, WALI, its characteristics and uncertainties, the level 2 temperature product of IASI and the forecast and reanalysis outputs of ERA5. In Section 3, the sequences of measurements are displayed and discussed with regard to synoptic weather conditions. Then, the coherence between the lidar and modelling outputs are presented in Section 4. Section 5 focuses on presenting the results of the inter-comparison with IASI. Finally, these results are discussed, and conclusions are drawn in Section 6. Three appendices are attached at the end of the article: Appendix A briefly presents the major ETEs that occurred in metropolitan France since the 1950s; Appendix B describes the signal processing and calibration of a PRR lidar and the particular case of WALI with its error budget; and Appendix C details the statistical indicators used for the inter-comparisons.

2 | INSTRUMENTS AND MODELLING

In this section, we present the different tools used to sample the atmosphere and model the behaviour of the meteorological atmosphere.

2.1 | Rotational Raman lidar

The basis of temperature measurements by the PRR technique is the asymmetric variation of the intensity of rotational Raman lines of the two main atmospheric gases (nitrogen and oxygen) spectrum with the thermodynamic temperature (Cooney, 1972). A description of the measurement method can be found in various scientific literatures (e.g. Behrendt et al., 2004; Behrendt & Reichardt, 2000). The reader can find details on the PRR

signal processing, the calibration, and the uncertainties assessment procedure in Appendix B.

2.1.1 | Presentation of the lidar

The WALI system used in this study is a compact and transportable lidar nominally emitting ~100 mJ at 355 nm in eye-safe conditions. The overlap function of this lidar is short (~200 m) and can be assessed experimentally for lidar signal correction (down to an overlap of 80%). Hence it allows to perform reliable measurements at low-level altitudes critical for air quality and meteorology purposes (e.g., 300 m AMSL or ~140 m above ground in this study). A recent study of Totems et al. (2021) describes in detail the instrument along the sources of bias for Raman measurements and processes for mitigating their impact. The laser has now been frequency-stabilized and dedicated rotational Raman channels have been added. The two PRR reception channels in the WALI system are centred at the two distinct wavelengths of 354.09 and 353.22 nm on the anti-Stokes side of the Raman spectrum. For these channels, the characteristics of the narrow interference filters are specified following studies conducted by Hammann and Behrendt et al. (2015). A high rejection of the emitted wavelength λ_l was prescribed to avoid contamination by the elastic scattering signal backscattered from aerosols and clouds. Also, the commercially available tripled Nd: YAG laser used in WALI (Q-Smart 450 system manufactured by Lumibird, formerly Quantel) was modified by the manufacturer who added a fibre laser injector to stabilize the wavelength at $\lambda_l = 354.725$ nm in vacuum, at the cost of a pulse energy reduction from 120 to 100 mJ. The native resolutions used in routine observations are 0.75 m and ~1 min (1000 profiles for a 20 Hz pulsed laser). During the processing, the signal is low-pass filtered to improve the signal-to-noise ratio and achieve a final vertical resolution of 50 m, suitable for the purpose of this study. Like water vapour measurements, the derivation of the atmospheric temperature by PRR lidar requires a reliable calibration against external in situ data. When operating at Laboratoire des Sciences du Climat et de l'Environnement (LSCE), the more convenient external data are the radiosondes profiles available 14 km of the lidar site at the Trappes Météo-France station.

2.1.2 | Temperature uncertainties

Among the WMO observational breakthrough requirements, the one for high-resolution forecasting is set for atmospheric temperature to 1°C of uncertainty within both the PBL and the free troposphere (FT) associated with vertical resolutions of 250 m (PBL) and 450 m (FT) and a temporal resolution of 30 min. Having this objective in sight, the error budget of the WALI can be detailed.

Uncertainty sources are plural, they can arise from the environmental conditions where the instrument is embedded, from the different elements of the acquisition chain (e.g., shot noise) and the calibration procedure. One should note that a significant drift of the central wavelength of the interference filters (>1 pm) or the laser emission line would be critical for lidar temperature measurements. As such a drift could be the consequence of the ambient temperature variability, it must be strictly stable and kept within a ± 1°C interval around the working temperature set at 22°C for the WALI system. Moreover, the laser power, its pulse frequency or the duration of temporal profile integration are, at the first order, the parameters driving the altitude range reachable by the lidar with a signal-to-noise ratio sufficient to retrieve the temperature within a 1°C error. The calibration function, although being only an approximate of the analytical expression of the dependence of the ratio of the two PRR channels with the thermodynamic temperature (see Appendix B), has a very low intrinsic error (<0.1°C). Nevertheless, a great care must be taken when calculating the calibration constants using lidar profiles and concomitant exogenous temperature profiles of reference. Indeed, this calibration must use parts of the lidar profiles with low noise while being out of the overlap function influence zone. For the WALI system, this zone can be taken from ~0.5 to 3 km for daytime measurements and up to 6 km at night. For this study, the WALI was calibrated afterwards once for each period using all available radiosondes.

Table 1 summarizes the error budget of the WALI for the two periods discussed in this work. The experimental error budget is assessed from a comparison with 28 concomitant radiosonde profiles (13 days and 15 nights). It appears that the bias is low and the centred root mean-square error (RMSE) < 1°C except for the daytime RMSE between 1.5 and 3 km (here the RMSE is centred while the root-mean square deviation, RMSD, is not de-biased, see Appendix C). Indeed, a difference is observed between lidar data and radiosoundings near the PBL top. The uncertainties deduced from simulations (RMSD) are quite lower than the RMSE found experimentally, mainly in the lower troposphere. We suppose that the natural variability between the lidar location and the Trappes station may be an important part of these discrepancies. In the simulation, such natural variability is not accounted for.

Figure 1 displays two examples (night and day) of lidar profiles after calibration during the winter 2018

TABLE 1 Overview of the mean bias (MB, see Appendix B) and the centred root men square error (RMSE, see Appendix B) of the lidar system, with reference to radiosounding and averaged into four altitude ranges

| | Experimental | | | | Simulation | |
| | Night-time | | Daytime | | Night-time | Daytime |
Altitude range (km)	MB (°C)	RMSE (°C)	MB (°C)	RMSE (°C)	RMSD (°C)	RMSD (°C)
0–1.5	−0.22	0.77	−0.02	0.81	0.02	0.2
1.5–3	−0.19	0.73	0.06	1.17	0.06	0.5
3–4.5	0.02	0.89	−0.45	1.9	0.1	2.5
4.5–6	−0.02	0.86	-	-	0.3	-

Note: These experimental results can be compared with the results of the simulations detailed in Appendix A (RSMD, see Appendix B).

FIGURE 1 Time series, from 22 to 27 February 2018 (a) and from 26 July to 02 August 2020 (c), of atmospheric temperature profiles derived from the weather and aerosol Lidar (WALI) pure rotational Raman channels. White strips represent screened data due to the presence of clouds. Two selected profiles (black solid lines in 2D time series) are plotted along concomitant IASI overpasses (red) and ERA5 reanalysis output (green) for 24 February 2018 (b) and 27 July 2020 (d)
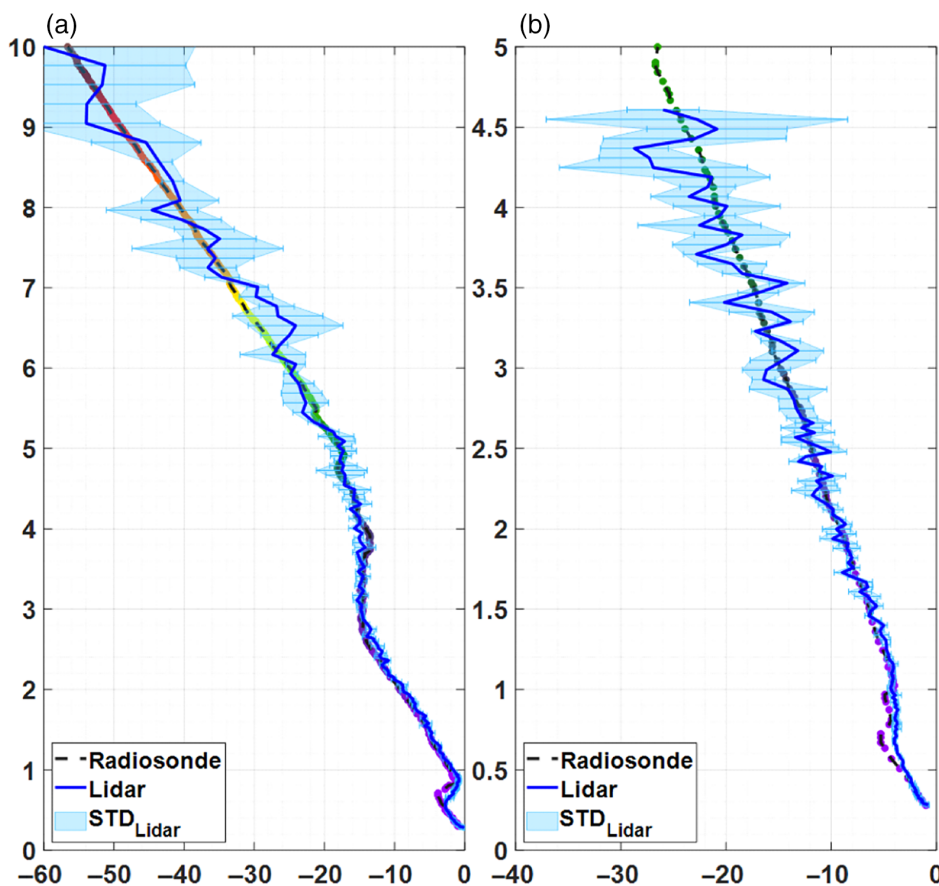
period. It shows a good agreement with the concomitant radiosoundings even with the drift away of the balloon in altitudes during the night.

One can note a difference, on both profiles, at about 700 m above the mean sea level (AMSL) where a temperature inversion occurs. Here, a natural variability of the PBL top and the entrainment zone is privileged to explain this gap due to the distinct location of the lidar and the radiosoundings station. Indeed, the lidar is located in a less urbanized area, which will probably result in a PBL development lower than near the Trappes station, which is more urbanized.

2.2 | IASI

The IASI is a spectroradiometer developed by the Centre National d'Etudes Spatiales (CNES) in collaboration with EUMETSAT. Three IASI instruments have been produced to be implemented on-board the MetOp (Meteorological Operational) platforms (A, B and C). Started in 2006 with the launch of MetOp A, this series takes part of the EUMETSAT Polar System (EPS), the European contribution to the Initial Joint Polar System (IJPS) initiated together with NOAA (Klaes et al., 2007). Flying in a sun-synchronous low Earth orbit at 817 km

above surface, MetOp platforms deliver detailed observations twice a day (at mid-morning and afternoon) between a $\pm 81.3°$ latitude range for any longitude in the world. MetOp A and B platforms have outlived their original life expectancy and are examples of great successes in spaceborne Earth observations, both for operational meteorology and long time series for climate studies. Among the passive instruments flown on these satellites, IASI is a keystone for temperature and humidity retrieval (e.g., Lerner, 2002), measurements of trace gas species such as CO, O_3, CH_4, N_2O and CO_2 (e.g., Chazette et al., 1998; Clerbaux et al., 1998) and also dust-like aerosols (e.g., Cuesta et al., 2020). Based on a Michelson interferometer measuring in the infrared, IASI split the 3.62–15.5 µm spectrum into 8461 channels with a resolution of 0.5 cm^{-1}. Perpendicularly to the satellite orbit track, IASI scans 30 successive elementary fields of view (EFOV) between $-48.3°$ and $+48.3°$ from the nadir, leading to a ground track of ~2200 km wide. Each EFOV includes four instantaneous fields of view with a footprint of 12 km at sub-satellite point, corresponding to the order of magnitude of the horizontal resolution of the instrument.

Data collected from EPS/MetOp are transmitted to the EPS core ground segment to produce operational outputs and in particular the IASI Level-2 products (Schlüssel et al., 2005) of version 6 (August et al., 2012). After an optimal cloud-screening of the geophysical scene observed by IASI, temperature profiles are retrieved using a set of statistical tools. Both a linear empirical orthogonal function (EOF) method or a non-linear artificial neural network (ANN) can be applied on the IASI brightness temperature spectrum or parts of it. The profile obtained is either the final level 2 product or the first guess used as input of an optimal estimation method (OEM). Finally, the vertical temperature profile is provided under cloud-free conditions on a 90-level grid extending between 0.005 and 1050 hPa (August et al., 2012). The vertical resolution is characterized by the averaging kernel functions associated with the retrieved profile. The peak of each averaging kernel gives the altitude of maximum sensitivity at each retrieved level, whereas its full width at half maximum can be interpreted as the vertical resolution of the retrieval (Clerbaux et al., 2009). The integration of these functions along the vertical tends to one when the information in the final product is coming from measurements and is <1 when a part of the first guess is still present. In the lower troposphere, the vertical resolution is typically between 1 and 2 km for IASI temperature profiles. Yet, some issues near the surface (e.g., the low thermal contrast between skin surface temperature and the first layers of the atmosphere) prevent accurate measurements below 2–3 km. Indeed, while the statistical error of the IASI temperature retrieval is about 0.6°C between ~2

and 9 km (800–300 hPa), it rises up to 1.5°C close to the tropopause and 2°C near ground level, as assessed with dedicated comparisons against radiosondes (Pougatchev et al., 2009). The bias oscillates within $\pm 0.5°C$ between 500 and 15,000 m (950–100 hPa). Another study conducted comparisons of IASI profiles with radiosondes in Asia (Kwon et al., 2012), the results for above-land retrievals suggest a larger bias and RMSE, up to 2 and 5°C, respectively.

For the comparison between IASI and the WALI presented hereafter, we considered the IASI pixels closer than 50 km from the lidar location. Plotted profiles are then the mean values enveloped in the associated standard deviations on these products.

2.3 | Modelling outputs

In this study, both forecasts and reanalysis from ECMWF are used. This section presents these products and the related bibliography.

2.3.1 | IFS forecasts

The IFS is the result of joint efforts from ECMWF and Météo-France to develop a general circulation model dedicated to weather prediction (Déqué et al., 1994). IFS has evolved, and the complete documentation can be followed-up on the ECMWF website (https://www.ecmwf.int/en/publications/ifs-documentation). Nowadays, the forecasts are computed following the operational procedure presented in Figure 2. From 0900 to 2100 UTC, there are 12-h 4D-Var assimilation windows that follow one after the other. In the same time frame, 3 h before the end of each assimilation window (0600 or 1800 UTC), a short forecast run is launched for 18 Forecast Steps (FS) of 1 h. It should be noted that more than half of the assimilated observation comes from spaceborne measurements and in particular IASI data (Collard & McNally, 2009).

In this work, we used the two forecast products of the CY42R1 version of IFS, which serves as basis for the ERA5 reanalysis (for details on the physical processes, refer to https://doi.org/10.21957/tr5rv27xu). In the following comparisons we used all the forecast steps (i.e., an hourly output) on 32 model levels up to 3 km (out of 137 levels) with a 0.25° horizontal resolution. The forecast outputs starting at 0600 UTC are associated with most daytime measurements of the lidar, and the forecast of 1800 UTC is more associated with night-time lidar measurements.

ECMWF temperature forecasts have been assessed in the literature and one can note the study of Wong
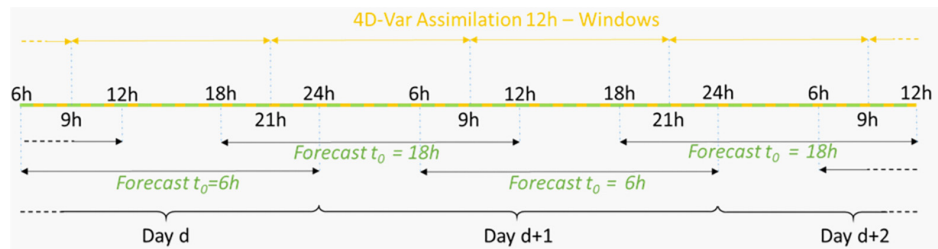
FIGURE 2   Diagram of the production procedures for the IFS operational forecast outputs. Two distinct products are available: A forecast run launched at $t_0 = 0600$ UTC and one at $t_0 = 1800$ UTC, both for 18 h/forecast steps (green). At the same time, assimilation windows occur every 12 h for a duration of 12 h

et al. (2015)) where they used radiosondes as reference. Their findings highlight a centred bias in the low atmosphere with a slight cold bias in the PBL of about one-tenth of a Kelvin and an RMSE between 1 K and 1.5 K, the latter being encountered close to the surface.

2.3.2 | ERA5 reanalysis

ERA5 reanalysis is the fifth generation of ECMWF global reanalysis. This product widely used, in particular in the atmospheric science community, is comprehensively presented by Hersbach et al. (2020). Unlike operational products, ERA5 reanalysis are computed a posteriori using the forecast outputs above mentioned and the maximum available observations. This way, each hourly data provided has ingested even more observations than the analysis used in IFS. Like the IFS forecasts, this hourly product comes with a 31 km horizontal resolution and up to 137 model levels from surface to 1 hPa. Hereafter, the model level product is used for comparisons with lidar data, while pressure level outputs (37 levels) are used to plot synoptic maps helping the understanding of the air mass circulations.

For both forecasts and reanalysis, an inverse-distance weighting average is made over the nine grid points surrounding the lidar location (48.711°N, 2.149°E) to obtain modelled temperature profiles collocated with the lidar. As the Parisian basin orography does not argue towards strong heterogeneities of the modelled temperature field, this interpolation method is expected to enhance the model representativeness on the lidar location compared with a comparison with the nearest grid point.

For its part, ERA5 is expected to be more accurate having assimilated a large number of observations. Still, the state-of-the-art 4D Var assimilation scheme cannot compensate for all forecast inaccuracies, whereas the different assimilated data sets are also associated with various degrees of confidence. As an example, Johannsen et al. (2019) highlighted that during summertime in

Portugal and Spain, although better than ERA-interim, ERA5 shows a cold bias for the modelled land temperature. Noh et al. (2016) used radiosonde observations from the Global Climate Observing System (GCOS) Reference Upper-Air Network (GRUAN) to assess ECMWF reanalysis (ERA-I at that time) in Korea. They found a temperature bias within ± 0.5 K along the atmospheric column and an RMSD between 1 K and 1.5 K in the PBL and tending to 0.5 K in the FT. Unexpectedly, in the literature, few articles assess the accuracy of ERA5 temperature profiles. However, one can note the work of Bouillon et al. (2020) who assessed IASI temperature retrievals against ERA5. They found differences of 1 K–5 K in the upper air but with a decreasing bias since 2015 in mid-latitudes (<2 K).

3 | TEMPORAL SEQUENCES OF OBSERVATIONS

In this section, the lidar observations are presented in parallel with the ERA5 outputs to describe the observed ETEs. We show how to determine a relevant time window for the temporal averaging of lidar-derived temperature vertical profiles used for comparison with the ones retrieved from both IASI and modelling. Synoptic maps are later presented to understand the time-altitude temperature variability.

3.1 | Lidar and ERA5

3.1.1 | The winter 2018 event

In Figure 3a, lidar-derived temperature is shown in colour from 22 to 27 February 2018 up to 3 km AMSL. This 5-day period contains strong vertical and temporal temperature gradients. Several features can be detailed based on these observations. First, the diurnal cycle of the temperature in the PBL is clearly noticeable. The
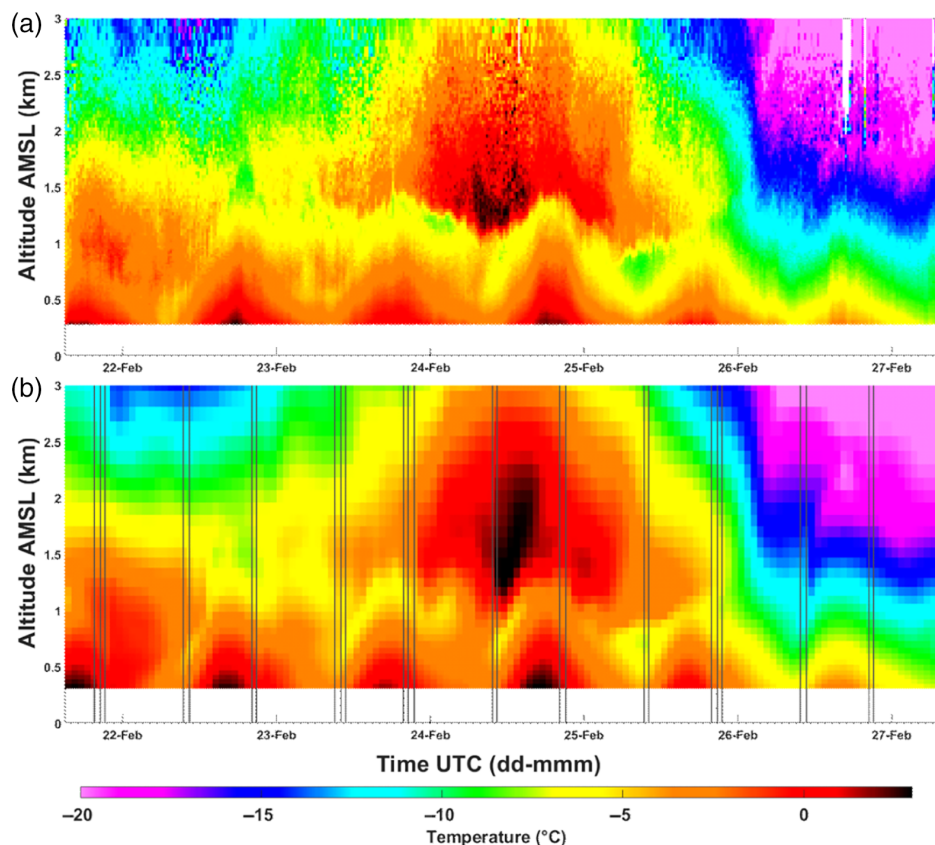
FIGURE 3 Time series, from 22 to 27 February 2018, of atmospheric temperature profiles derived from: (a) lidar and (b) ERA5 reanalysis. Times of IASI overpasses are indicated by thin black lines on the bottom panel. White areas in the top panel correspond to rejected data due to cloudy conditions

development of the PBL is decreasing in altitude during this period subsequently to the settlement of a high-pressure system triggering a cold wave perceptible at the end of the dataset (purple area). In the middle of the dataset, just above the PBL top, a warm air mass is advected. This atmospheric situation leads to a strong temperature inversion ($+10°C/300$ m) at ~1–1.5 km AMSL on 24 February 2018. On the night of 25 February to 26 February, the temperature at 2 km drops by 15°C with a Siberian air mass surging over Western Europe. The resulting vertical gradient of temperature of $-10°C/$ km contrasts with the $-5°C/$km gradient that occurred during the un-disturbed period of 22 February to 23 February, in line with seasonal norms. It is worthwhile to note that although the temperature field is disturbed and unstable (especially in the middle of the dataset) the whole period remains cloud-free. This clear sky may result from a particularly dry air and a subsidence induced by the anticyclonic conditions prevailing over the Paris area.

Figure 3b represents the same time-height temperature cross-section but from the ERA5 reanalysis. The two datasets match very well. Some differences can still be noticed: an over-evaluation of the temperature by the model, in particular in the PBL during the afternoon and in the overhanging warm air mass. The discrepancies are

to be detailed in profile-to-profile comparisons presented hereafter between the WALI, IASI (overpass times highlighted in thin black lines in Figure 3b) and models.

3.1.2 | The July 2020 event

As for the previous dataset, in Figure 4a, lidar-derived temperature is shown in colour from 26 July to 02 August 2020 (8 days) up to 3 km AMSL. More clouds perturbed the lidar observations than during the winter event and even some rains are highlighted where the white area connects with the blind area of the lidar. In this case too, one can see the diurnal cycle of the PBL. From this summer typical cycle, with afternoon temperature up to ~25°C, two anomalies stand out: a first little heat stroke was felt on 27 July in the afternoon with surface temperature above 30°C and finally a short but intense heatwave from 30 July to 1 August. On this last event, surface temperatures in the Parisian basin were above 35°C and approached 40°C on 31 July, without any night cooling. This warm air mass develops high in altitude with a 2 km temperature around ~20°C to be compared with the ~5°C recorded 2 days before on 29 July at the same altitude. Rainfall finally ends the heatwave on the morning of 1 August.
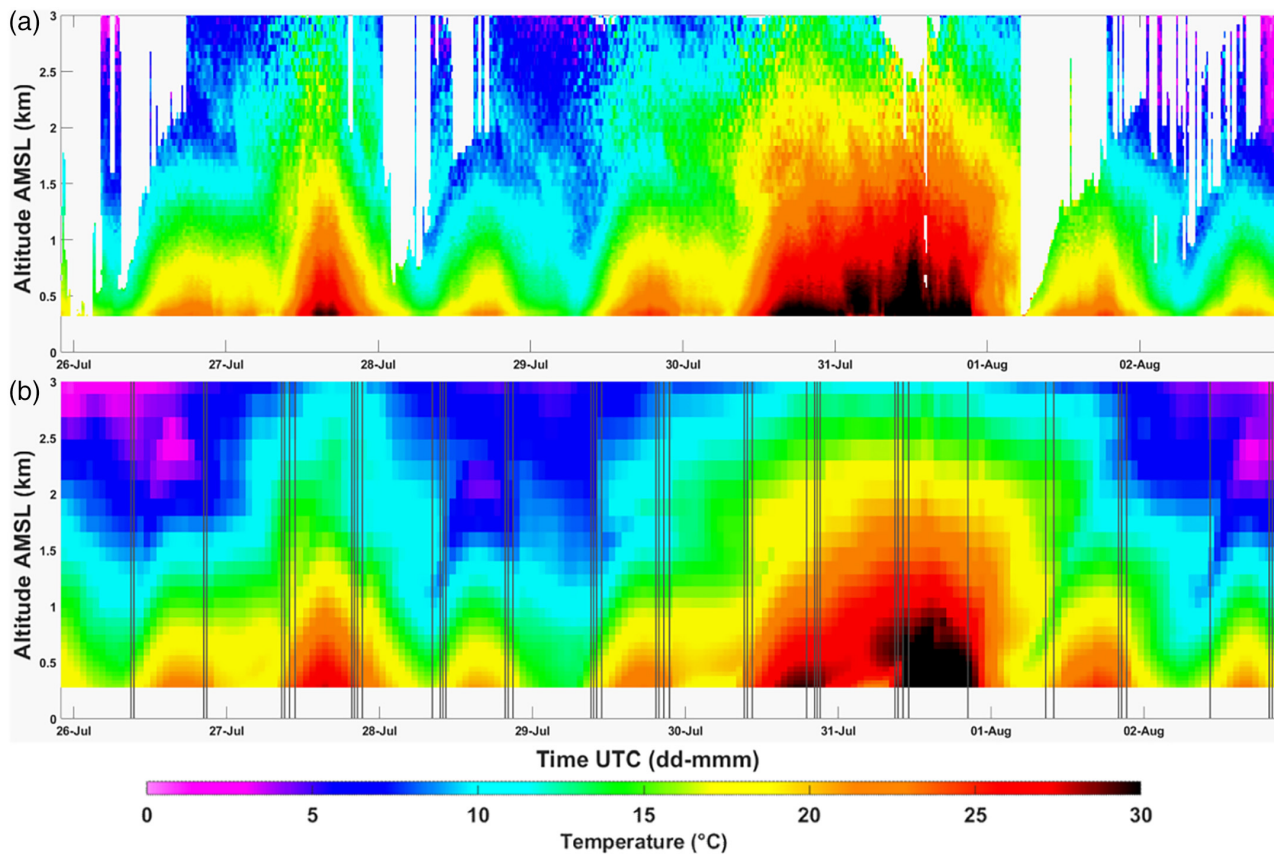
FIGURE 4 Same as Figure 3 for 26 July to 02 August 2020. Figures 3 and 4 Have the same scale

Figure 4b represents the temperature extracted from the ERA5 reanalyses. Again, the model captures the temperature field quite well in general. However, in contrast to the winter period, we tend to see an underestimation of the modelled temperature. Indeed, during the two warm periods, lidar observations retrieved warmer temperature near the surface, also associated with a higher PBL development (the yellow coloured part exceeds 1.5 km on 27 July according to the WALI but not for ERA5). Furthermore, some temperature inversions seen on the lidar records, in particular on 28 and 29 July between 1 and 2 km, are not well pictured from the reanalyses. As for the winter case, IASI transits are plotted above the temperature field in Figure 4b and a quantitative comparison is presented in Section 4 to better highlight the discrepancies.

3.1.3 | Temporal averaging

Drawing conclusions from profile-to-profile comparisons can be a delicate task when the datasets compared have different resolutions, and in particular different time steps. Such a comparison with lidar data does not necessitate the high temporal resolution associated with this instrument and a decrease of its temporal

resolution using a low-pass filter can enhance its altitude range and accuracy. However, depending on the averaging time window considered, discrepancies can arise from the natural variability within this time window. In order to reduce the natural variability effect on our comparisons, we have defined a threshold on the statistical indicator ξ used by Behrendt et al. (2015) and defined by:

$$\xi(\tau) = \sqrt{< (T(t+\tau) - T(t))^2 >_t} - \xi_0, \quad (1)$$

where τ is the delay, t the time, T the lidar-derived temperature and ξ_0 the value of ξ for a null delay. $<X>$ represents the time average on the variable X.

Computing this indicator along the vertical allows to assess the typical variability of the temperature vertical profile within period τ. The result is presented in Figure 5 for the cold wave period (CW, Figure 5a) and the heatwave period (HW, Figure 5b).

An expected phenomenon stands out in this figure: the temperature is more stable in mid-latitude winter with a lower temperature amplitude over 3 sliding hours than in summer. One can notice a remarkable pattern between 1–1.5 km (Figure 5a) and 1.5–2 km (Figure 5b).
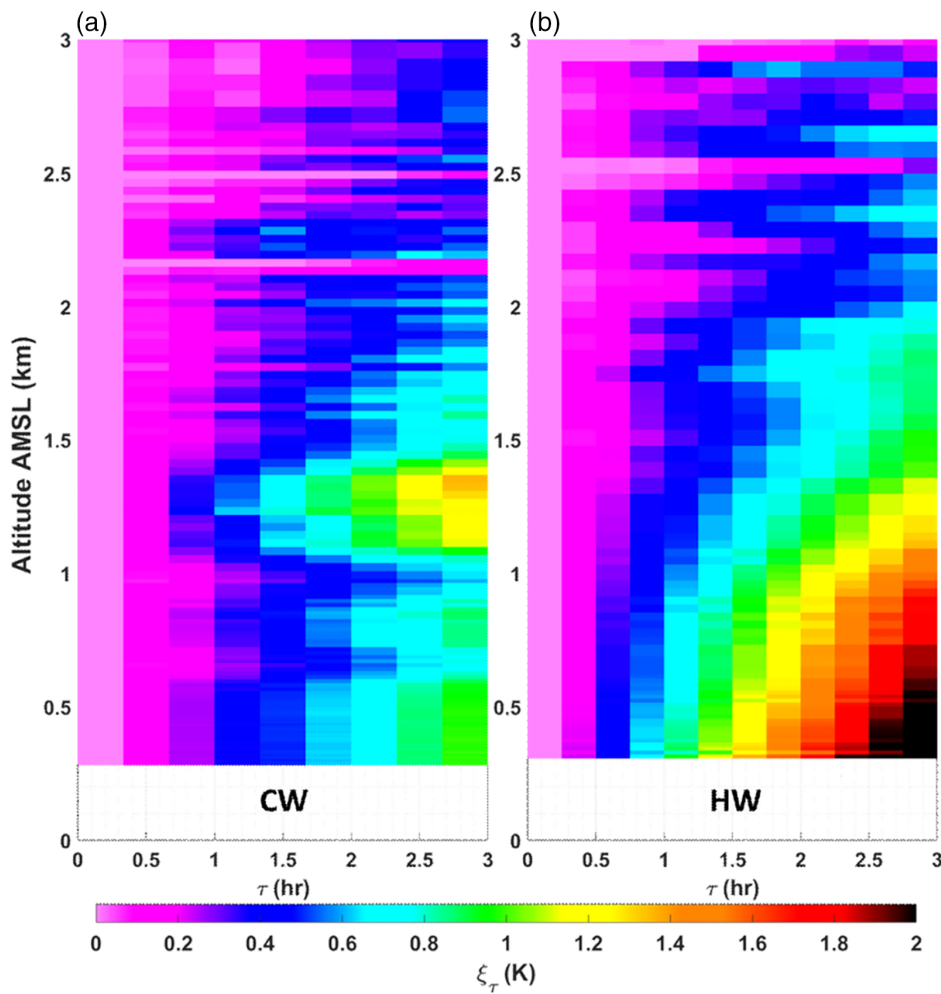
FIGURE 5 Delay-height cross-section of the indicator ξ assessing the temperature stability of the atmosphere. The calculation is performed up to 3 h of delay up to 3 km of altitude both for the cold wave (CW, a) and the heatwave (HW, b) periods
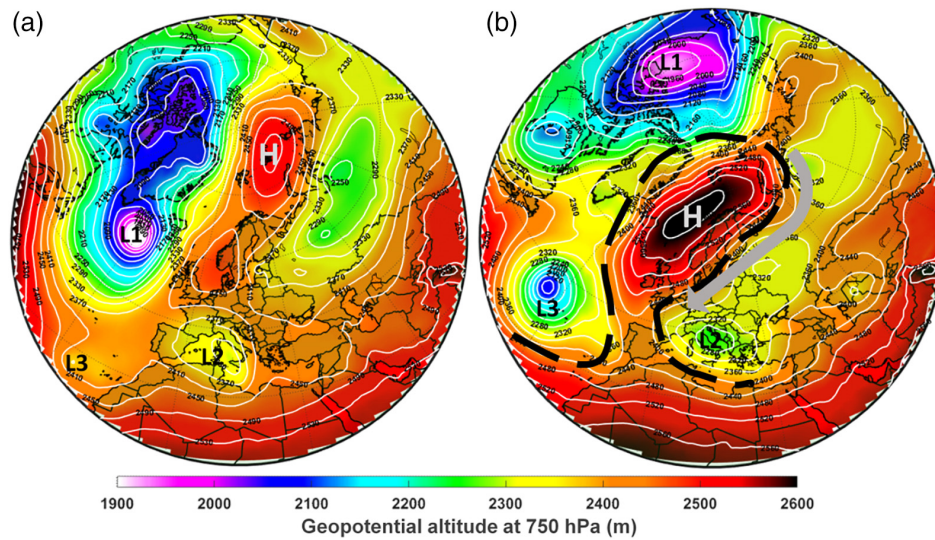

FIGURE 6 ERA5 geopotential altitude at 750 hPa above Europe on 23 (a) and 26 February 2018 (b) at 1200UTC. The lows are named L1 (Icelandic low), L2 and L3 to highlight their migration within 3 days, H depicts the position of the Siberian high. The thick black dotted line in (b) emphasizes the omega-type blocking and the associated southwesterly flow (grey arrow)

This enhancement of ξ at these altitudes can be associated with the PBL top and the temperature variability in the entrainment zone. It is worth noting that the high temporal resolution of lidar measurements is necessary

to perform such calculation on the temperature field. In order to remain below the 1°C uncertainty threshold, and considering the variance related to the lidar signal, the threshold of $\xi < 0.2$°C for the natural variability is a fair

compromise. It requires a time-averaging window of 30 min that will be used in the following.

3.2 | Meteorological context

The atmospheric conditions that favoured the development of the studied heat and cold waves will be described in this subsection.

3.2.1 | Origin of the late February 2018 cold wave

Although the 2018 event is mild compared with historically significant CWs in France (see Appendix C), its origin does not differ from common cases. The following discussion on the synoptic weather pattern before and during the CW relies on the ERA5 reanalysis product (cf. Section 2.3.2). Reanalyses show the establishment of a low–high dipole above the Artic from 21 to 23 February (Figure 6a). During the 3-day period from 23 to 25 February, the high strengthens and stretches from northern France to the Kara Sea with an oval shape centred southeast of the Svalbard Islands. On 26 February, the situation evolves towards an omega-type blocking pattern as shown in Figure 6b, where the strong high is surrounded by two lows, one above the Azores Islands and another one above the Balkans. This blocking system leads to a corridor during its settlement, informally called 'Moscow-Paris', through which Siberian air masses are pulled southwestward (grey arrow in Figure 6b).

If the atmospheric blocking explains the surging Siberian air from 26 February, the low L2 above Sardinia is at the origin of the warm air mass identified in Figure 3 on 24 and 25 February. This low-pressure system lifts Mediterranean air above the Alps and brings it towards western France. The shift to the right of L2 and the settlement of H leads to the strong temporal gradient of temperature observed during the night from 25 to 26 February where the temperature at 2 km drastically decreases by 12°C in 12 h.

3.2.2 | Origin of the July 2020 heat wave

For the heatwave event, the synoptic maps are restricted to the extra-tropical region centred above Western Europe, excluding the North pole. By the end of July 2020, a quasi-stationary Azores high protrusion settles around the Gibraltar Strait (H in Figure 7). The presence of the Icelandic low (successively L1 and L2 in Figure 7) heading East induces the common westerly flow above France associated with mild oceanic air masses (Figure 7a). The oscillating position of H leads on 27 July to a rise of temperature observed in Figure 4. Then, the L1 motion from 28 to 31 July causes the attraction of H towards Central Europe, while L2 strengthens a high-pressure ridge emerging along a Spain–Norway axis (grey arrow). This pattern presented in Figure 7b could be interpreted as an inverse omega block; it brings warm air masses from the Iberian Peninsula while preventing any strong winds, cloud development and permitting heat to build up in Europe. After 1 August, the high-pressure ridge vanishes and H retracts off the coasts of Portugal. The temperature drops to seasonal norms.

4 | RESULTS

In the following, the forecasted and reanalysed temperature fields are checked against WALI-derived vertical profiles of temperature. We focus on specific profiles to bring out discrepancies between ERA5 outputs, IASI- and WALI-derived temperature profiles.
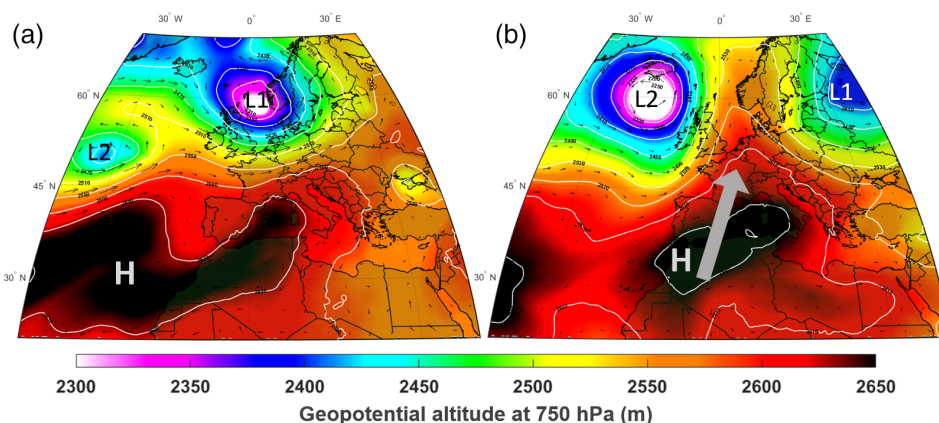

FIGURE 7 Same as Figure 6 on 28 (a) and 31 July 2020 (b) at 1200UTC. H depicts the Azores high
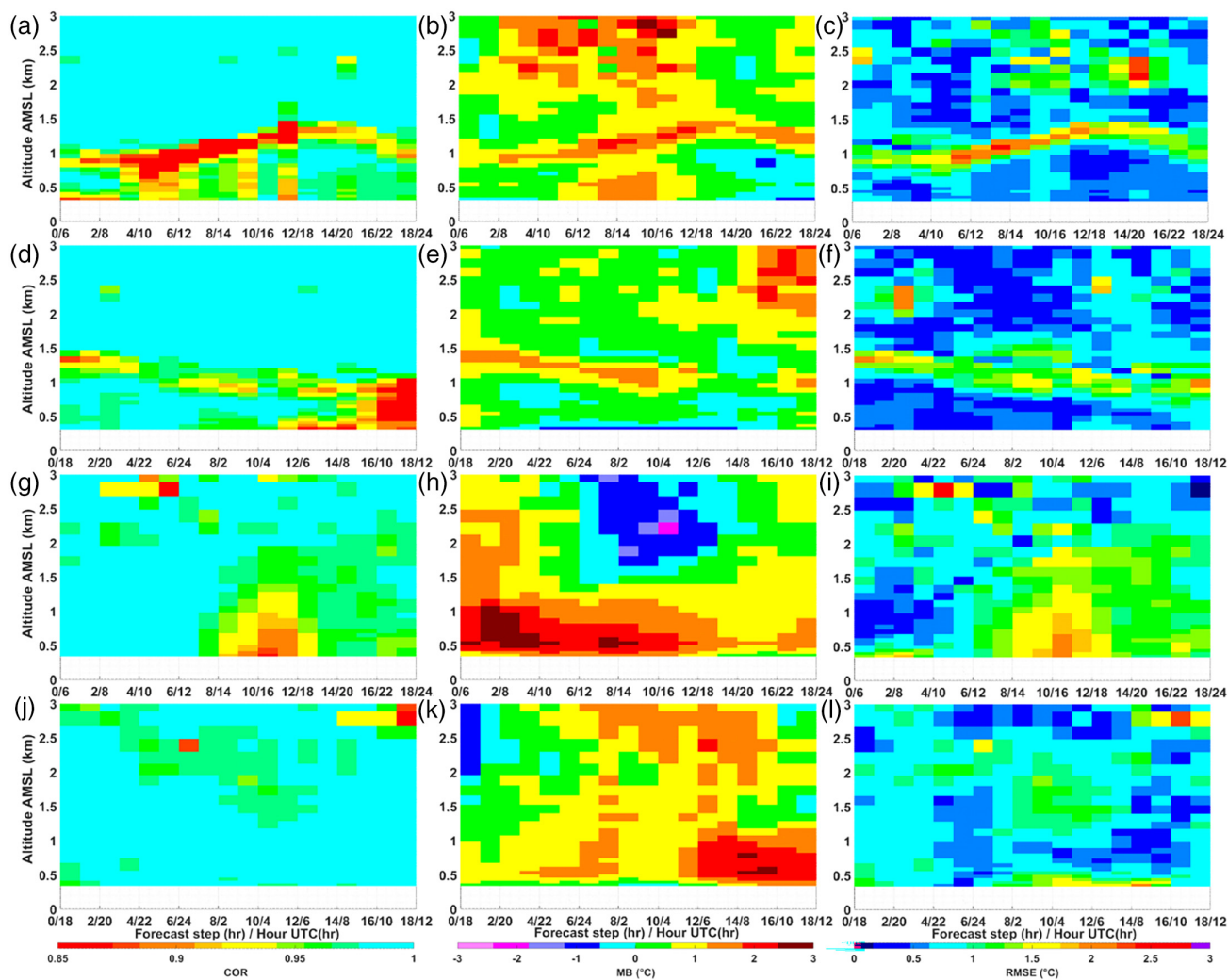
FIGURE 8 Forecast step – Altitude cross-section of the three statistical indicators used to compare the lidar-observed temperature field with the forecasted ones (model – lidar). The left column (a, d, g, j) refers to the correlation (COR), the middle one (b, e, h, k) to the mean bias (MB) and the right one (c, f, i, l) to the centred root-mean-square error (RMSE). The six first panels (a, b, c, d, e, f) are related to the winter event, the three firsts are calculated against the 0600 UTC forecast and the three others with the 1800 UTC forecast. The last six panels (g–l) are related to the summer 2020 period with the same protocol

4.1 | Consistency between lidar-derived and modelled temperature profiles

Figure 8 summarizes the comparisons computed between WALI data and the two forecast outputs detailed in Section 2.3.1. For each forecast step (corresponding to a different time of the day, depending on whether it is the 0600 UTC or 1800 UTC forecast), the statistical indicators detailed in Appendix B are calculated: (i) the correlation (COR), (ii) the mean bias (MB), and (iii) the centred root-mean-square error (RMSE). This way, we can assess if a drift, synonym of forecast quality loss, appears as the steps increase.

As shown in Figure 8, the forecasts offer a rather good match with lidar data. Indeed, for both meteorological situations, the COR exceeds 0.8 for any forecast step, the

MB is framed by the interval $[-3°C, +3°C]$ and the RMSE does not top 3°C. Despite this overall good agreement, MB and RMSE values are higher than expected in the light of previous findings (centred bias and up to 1.5 K of RMSE in Wong et al., 2015) and details on discrepancies can be outlined.

As shown in Figure 8g,i, the 0600 UTC forecast seems to lose quality with time during the HW period. It is noteworthy from step 8 to 18 up to 2 km with a maximum corresponding to the end of the afternoon. This is less the case during the CW period where this drift could be partially masked by the model difficulties to reproduce the temperature cycle in the PBL. Indeed, as referenced in section 2.3, models still struggle to adequately represent the PBL dynamics in stable and neutral conditions. This translates in our comparisons into a sharp decrease of the

COR in the PBL with respect to the high values in the FT (>0.95) for the CW case. Whether it is the COR, MB or RMSE, from the six first panels of Figure 8, the PBL top stands out, highlighting discrepancies between modelling and lidar profiles. For the HW case, no clear evidence emerges from Figure 8g–l regarding the PBL vertical structure.

Regarding model temperature bias, for the forecasts during both periods, the MB is most of the time positive (hotter modelled temperature). One exception could be noted during the HW period (Figure 8h, steps 6–8 to 18 and Figure 8k close to step 1) where a cold bias in the FT appears during the end of the afternoon/early
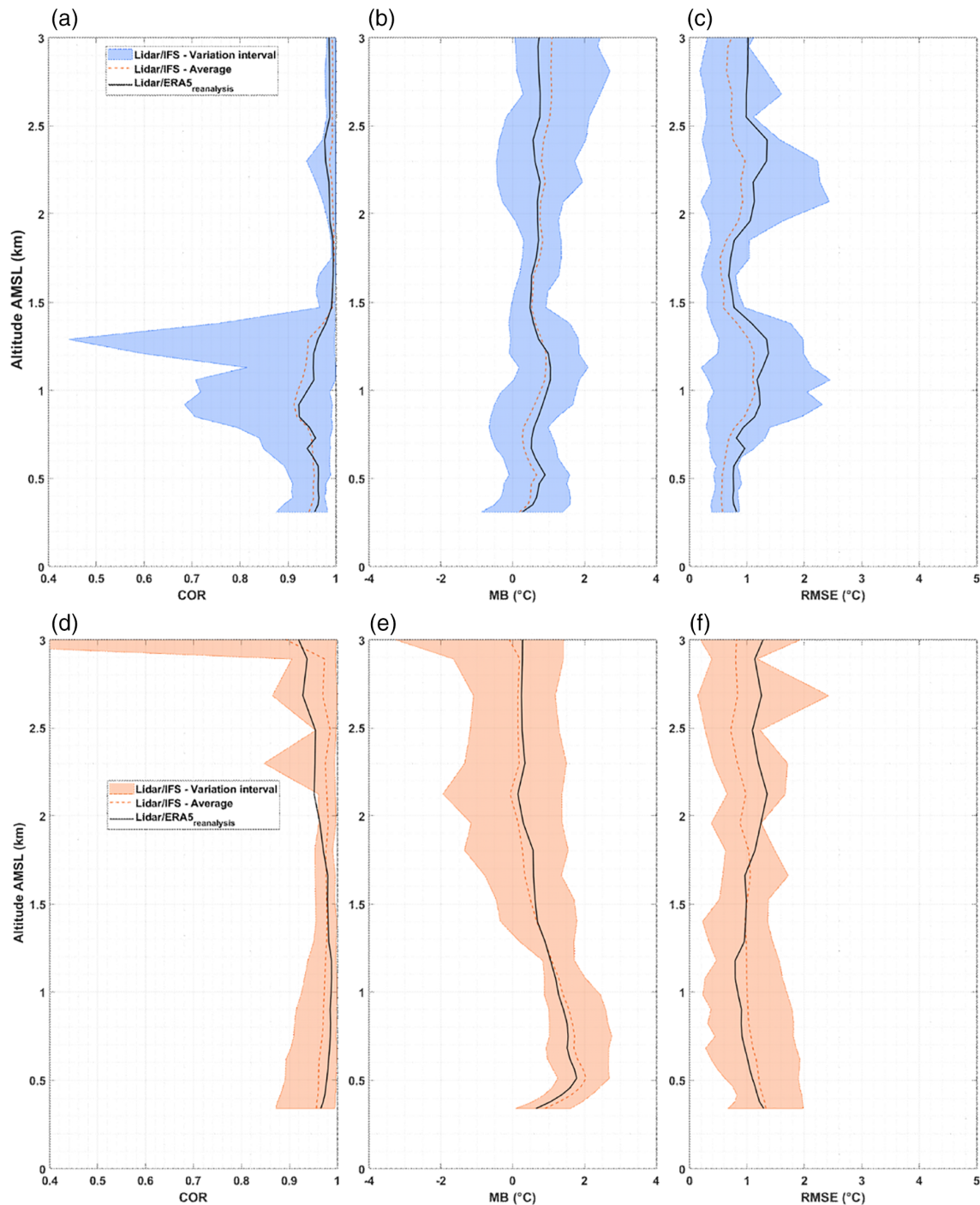

FIGURE 9 Profiles of statistical indicators between lidar observations and model outputs. Panels (a)–(c) display respectively the correlation coefficient (COR), the mean bias (MB) and the centred root-mean-square error (RMSE) for the cold wave period. Panels (d)–(f) are the counterpart for the heatwave period. The coloured areas represent the variability of each indicator during the forecast period
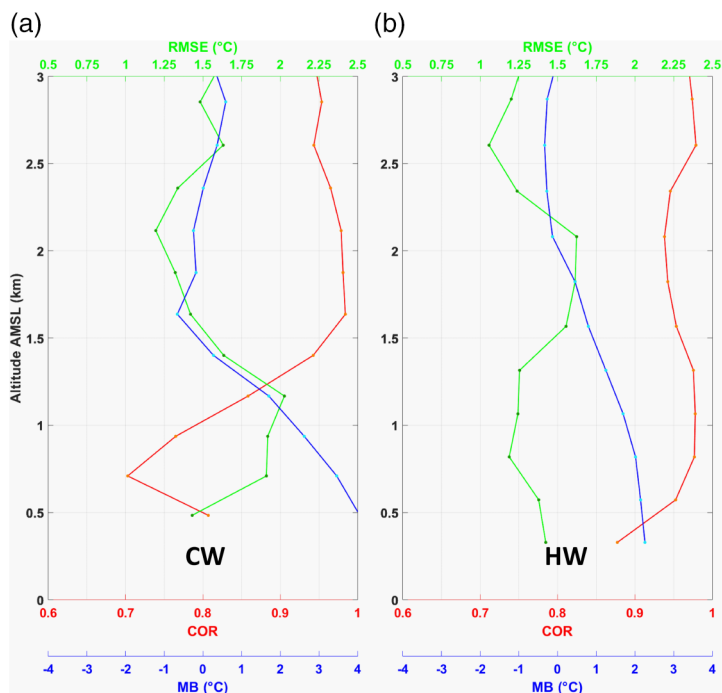
FIGURE 10 Profiles of correlation (COR, red), mean bias (MB, blue) and centred root-mean-square error (RMSE, green) between IASI temperature profiles and corresponding lidar measurements: (a) for all the 26 lidar-IASI profiles of the cold wave period (CW), (b) for all the 48 lidar-IASI profiles of the heatwave period (HW)

evening. This cold bias may be the result of an underestimation of heat exchanges from surface and PBL to the FT during the HW period. On the same panels (Figure 8h,k), while a glance to Figure 4 might suggest an underestimation of the reanalysed temperature, forecasts tend to be quite much warmer in the morning PBL during the HW period. A closer look at Figure 4 reveals that while some of the strongest temperatures are underestimated near the surface (<0.5 km), in particular during the hot afternoons, forecasts tend to overestimate systematically the temperature between 0.5 and 1 km.

The indicators used in Figure 8 are averaged to build Figure 9 (dashed lines), showing the comparison between lidar-derived temperature and the forecasts (red dotted line). The variation interval is materialized by the coloured areas (in light blue). In the same figure, the comparison between reanalysis and WALI is plotted in black. The forecasts and the reanalysis are rather consistent in their comparison with the lidar-derived temperature. A better correlation is found for both the CW and HW in the PBL, up to 1.5 km AMSL. The MB and RMSE decrease also in this region but only for the HW case. It seems that the overestimation highlighted in Figure 8 might be mitigated through data assimilation. However, for the CW case, the MB (Figure 9b) is slightly greater for the reanalysis in the PBL and lower above 1.5 km AMSL. Furthermore, from surface to 3 km, the RMSE between WALI and reanalysis is significantly larger than with the forecasts. It is also significantly larger for the summer case above 1.5 km AMSL.

While the RMSE is of the same order of magnitude as expected in the light of previous study (Noh et al., 2016), the bias found here in the PBL is significantly higher (closer to 1 K in average than 0.5 K).

4.2 | Consistency between lidar- and IASI-derived temperature profiles

Over the duration of the measurements, 26 coincidences, that is, IASI-derived profiles above the lidar location, occurred during the CW case and 48 during the HW period. None of them were close to a radiosonde launch time due to the ascending node time, which is also why the continuous sampling of the ground-based lidar is an advantage.

4.2.1 | Statistical comparison

The COR, MB and centred RMSE profiles between IASI and WALI are plotted in Figure 10. The statistics on the 26 available profiles during the CW episode are shown in Figure 10a where IASI-derived vertical profiles of temperature are compared with the concomitant lidar datasets up to 3 km AMSL. In Figure 10b, the same computation is made for the 48 profiles of the HW measurement period.

During the winter case (Figure 10a), the correlation drops from ~0.95 to ~0.7 below 1.5 km AMSL, as well as the MB, which is within the [−1°C; +1°C] interval above
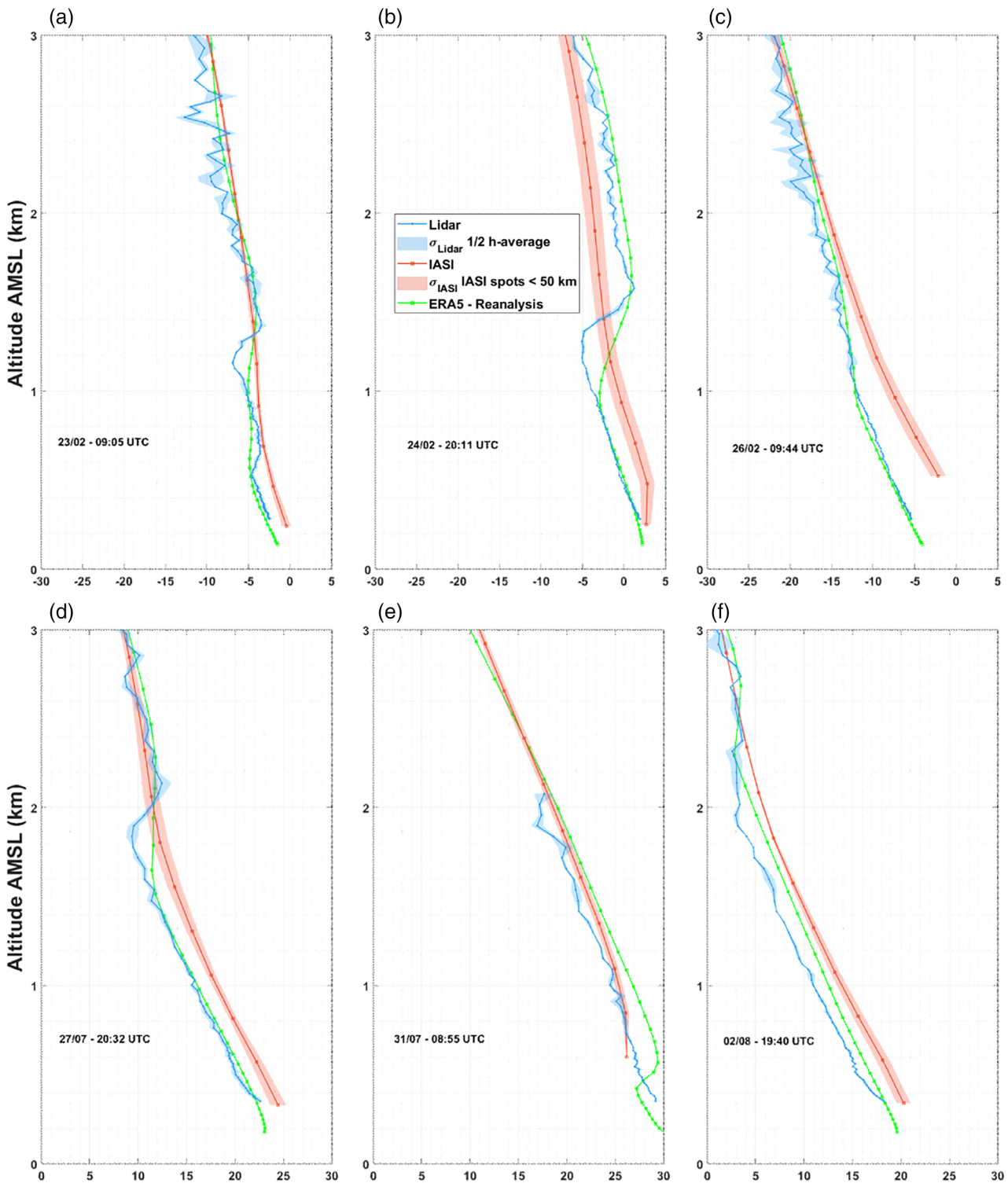
FIGURE 11 Profiles of IASI (red), WALI (blue) and ERA5 reanalysis (green). The profiles are plotted up to 3 km AMSL during six IASI overpasses, three during the cold wave period (a–c) and three during the heat wave periods (d–f)

1.5 km but about +4°C near ground level. The centred RMSE profile maxima show the altitudes where IASI commits unstable errors with reference to WALI. The altitudes between 0.5 and 1.5 km AMSL correspond to the PBL top height where temperature inversions are not correctly sampled by IASI. The RMSE is larger in the PBL (>2°C) and remains around 2°C in the FT up to 4 km AMSL.

On the other hand, during the HW (Figure 10b), we can notice a better consistency between IASI and WALI.

TABLE 2   Summary of the uncertainties of WALI computed experimentally against radiosoundings and the discrepancies calculated between WALI and ERA5, IFS and IASI datasets

Statistical indicator	Range (km)	RS/WALI	WALI/ERA5	WALI/IFS	WALI/IASI
COR	0–1.5	0.99	0.97	0.96	0.88
	1.5–3	0.99	0.93	0.98	0.96
MB (°C)	0–1.5	−0.12	0.97	0.80	2.2
	1.5–3	−0.06	0.52	0.61	0.01
RMSE (°C)	0–1.5	0.81	0.97	0.85	1.6
	1.5–3	1.0	1.3	0.89	1.4

The PBL altitude is higher, around 1.5–2.5 km highlighted with a slight increase of the RMSE (up to 1.5°C) and a little decrease of the COR (~0.97 to ~0.94). Above this PBL top altitude, the bias is centred around 0°C and below it reaches 2°C near ground, associated with a correlation still larger than 0.85.

Despite the fact that the larger number of available profiles during the HW (near twice as for the CW) could tend to smooth the statistical indicators, the operational temperature profiles derived from IASI seem to better apprehend the low troposphere structure when the PBL is more developed and presents smaller temperature inversions. As demonstrated, IASI does not capture sharp vertical temperature gradients, its profiles being too smooth. However, in the FT, where such gradients are not expected, WALI and IASI data sets present a good match.

It is worth noting that the IASI–lidar comparison results regarding bias are higher than expected, knowing the results of Pougatchev et al. (2009) and Bouillon et al. (2020) in the winter PBL (4°C > 2 °C, during the CW case) but conform in the summer PBL (~2°C) and in the FT (MB ~ 0.6 °C). These differences can be explained by the poor vertical resolution of IASI near the surface and up to 2 to 3 km.

4.2.2 | Discussion on representative cases

From all the IASI overpasses used to present the statistics in Figure 10, only six representative profiles are plotted in Figure 11. Three of them (a–c) are chosen during the CW and the three other during the HW. These profiles are not chosen randomly but around discrepancies observed between lidar and reanalysis in Figure 4. Thus, when available, the closest (>50 km) pixels of IASI are averaged (red line) and the standard deviation is represented by the shaded red area. The green curve is the reanalysis profile closest in time and the blue curve is the lidar-derived temperature profile averaged 30 min around the IASI overpass time.

The sharp temperature inversions that are measured by lidar, in particular those plotted in panels a, b, d and f of Figure 11, are not observed on IASI profiles and are incorrectly modelled in the reanalysis. Even though the IASI Level 2 products are re-gridded to obtain 11 levels between surface and 3 km, the physical resolution is related to the averaging kernels of each profiles and is between 1 and 2 km at low altitudes (<3 km). This explains the lack of sensitivity of IASI to these temperature inversions. Except for Figure 11b, where the temperature inversion is uncommonly strong due to the warm air mass above the PBL, IASI and reanalysis match quite well above 2–2.5 km. It should be recalled that IASI radiances are assimilated to obtain the ERA5 product through a 4D var assimilation scheme. Below, as expected from the literature, IASI is overestimating the temperature by several Celsius degrees (up to 5°C during the cold wave on 26 February 2018, Figure 11c). During the heatwave (Figure 11e), the IASI profile does not overestimate the temperature below 1 km and is below the ERA5 curve, in contrast to all the other cases plotted in Figure 11. It should be noted that cloudy conditions limited the lidar range to ~2 km. The IASI retrievals could have been affected by these conditions too.

On the same panel (Figure 11e), one can also notice a temperature inversion modelled by ERA5 close to the surface, which seems to not exist according to lidar observations. This feature can also be noted in Figure 4. While the ERA5 and WALI data are well related, this case is remarkable and astonishingly associated with the warm outbreak. The other cases of Figure 11 agree very well except near the PBL top, with temperature inversions that are smoother in ERA5. This smoother aspect recalls the results highlighted on the IASI profiles, which are too smooth to capture low-temperature inversions. It raises the question of a circulatory issue as ERA5 assimilates IASI radiances. However, the covariance matrix of IASI provided as an input in the assimilation process and carrying error estimates allows a graduation on the weight associated with IASI profiles. As a result, knowing

that IASI has an increasing error in the PBL, the assimilation process is expected not to take into account the IASI lowermost profile part. Hence, the apparent smoother PBL inversions in ERA5 than observed by lidar could be imputed to a lack of representation of complex physical processes of the PBL dynamics, which resonates with former studies such as that of Sandu et al. (2013).

5 | CONCLUSION

WALI's features allow temperature measurements with an uncertainty of less than 1°C within both the PBL and the lower/middle free troposphere (FT) (~3/6 km from ground for day/night), with a vertical resolution of 50 m and a temporal resolution of 20 min. Such capabilities meet the WMO observational requirements for the improvement of high-resolution forecasting and near-real-time forecasting. Hence, the lidar characteristics allow trustworthy and continuous temperature measurements in the PBL and the low troposphere with high temporal and vertical resolutions. These two case studies tend to demonstrate that a PPR lidar can be a reference tool in order to evaluate the representativeness of ETEs as reproduced by operational modelling and IASI spaceborne observation. The growing reliability of lidar systems and especially PPR lidars is about to allow to gather numerous and continuous datasets to serve as observational references and enter operational monitoring networks.

The uncommon CW that occurred in February 2018 and the flash HW at the end of July 2020 present ideal temperature fields to challenge the quality of both operational models and spaceborne observations. In each case, the synoptic situations are associated with an atmospheric blocking over Western Europe presenting large temporal and vertical temperature gradients as well as strong temperature inversions.

The results of the inter-comparisons presented in this paper show first an overall valuable concordance of forecast or reanalysis and lidar observations (COR >0.9 in average), which are summarized in Table 2.

It should be noted that the topography around the measurement site and the geographic situation of the Parisian basin do not argue for modelling difficulties linked to any orographic effects. Yet, as previously described in the literature, the winter PBL is poorly represented and temperature inversions, which have notable implications for air quality, are often underestimated (e.g., Royer et al., 2011). The IFS forecasts bias remains quite low but around 1°C warmer than lidar-derived temperatures and up to 2°C at low altitudes in late July 2020. Furthermore, the ERA5 reanalysis shows no significant improvement from forecast temperatures. IASI temperature retrievals show a warm bias (~2°C) under 1.5 km that can be larger than expected in some situation (>4°C); above the PBL, the bias is well centred and the correlation with lidar measurements is excellent.

In conclusion, this study shows the value of complementarity between passive spaceborne sounders like IASI and ground-based PRR lidar such as WALI to monitor the lower atmospheric layers. The ability of WALI to continuously trace the diurnal cycle of the PBL fills an observational gap and allows (i) to complement spaceborne instruments like IASI and (ii) to provide a strong constraint in the lower layers for meteorological models; in particular during ETEs. This capacity could benefit future spaceborne missions such as IASI-NG (Crevoisier et al., 2014) and the new generation of numerical forecast models (Brousseau et al., 2016) through data assimilation and parameterization validation (Flamant et al., 2021).

AUTHOR CONTRIBUTIONS
Alexandre Baron: Conceptualization (lead); data curation (lead); formal analysis (lead); investigation (lead); methodology (equal); software (lead); writing – original draft (lead); writing – review and editing (lead). **Patrick Chazette:** Conceptualization (equal); funding acquisition (lead); methodology (lead); supervision (lead); validation (lead); writing – original draft (supporting); writing – review and editing (supporting). **Julien Totems:** Data curation (equal); methodology (equal); supervision (supporting); validation (supporting); writing – original draft (supporting); writing – review and editing (supporting).

ORCID
Alexandre Baron https://orcid.org/0000-0002-0332-9579
Patrick Chazette https://orcid.org/0000-0002-6230-2982
Julien Totems https://orcid.org/0000-0002-1038-455X

REFERENCES

Adam, S., Behrendt, A., Schwitalla, T., Hammann, E. & Wulfmeyer, V. (2016) First assimilation of temperature lidar data into an NWP model: impact on the simulation of the temperature field, inversion strength and PBL depth: Lidar temperature data assimilation. *Quarterly Journal of the Royal Meteorological Society*, 142, 2882–2896.

Arshinov, Y., Bobrovnikov, S., Serikov, I., Ansmann, A., Wandinger, U., Althausen, D. et al. (2005) Daytime operation of a pure rotational Raman lidar by use of a Fabry–Perot interferometer. *Applied Optics*, 44, 3593–3603.

Arshinov, Y.F., Bobrovnikov, S.M., Zuev, V.E. & Mitev, V.M. (1983) Atmospheric temperature measurements using a pure rotational Raman lidar. *Applied Optics*, 22, 2984.

August, T., Klaes, D., Schlüssel, P., Hultberg, T., Crapeau, M., Arriaga, A. et al. (2012) IASI on Metop-a: operational level 2 retrievals after five years in orbit. *Journal of Quantitative Spectroscopy and Radiative Transfer*, 113, 1340–1371.

Aumann, H.H., Chahine, M.T., Gautier, C., Goldberg, M.D., Kalnay, E., McMillin, L.M. et al. (2003) AIRS/AMSU/HSB on the aqua mission: design, science objectives, data products, and processing systems. *IEEE Transactions on Geoscience and Remote Sensing*, 41, 253–264.

Balin, I., Serikov, I., Bobrovnikov, S., Simeonov, V., Calpini, B., Arshinov, Y. et al. (2004) Simultaneous measurement of atmospheric temperature, humidity, and aerosol extinction and backscatter coefficients by a combined vibrational–pure-rotational Raman lidar. *Applied Physics B: Lasers and Optics*, 79, 775–782.

Baron, A., Chazette, P. & Totems, J. (2020) Remote sensing of two exceptional winter aerosol pollution events and representativeness of ground-based measurements. *Atmospheric Chemistry and Physics*, 20, 6749–6768.

Behrendt, A. (2006). Temperature measurements with Lidar. Lidar: range-resolved optical remote sensing of the atmosphere. 273–305.

Behrendt, A., Nakamura, T. & Tsuda, T. (2004) Combined temperature lidar for measurements in the troposphere, stratosphere, and mesosphere. *Applied Optics*, 43, 2930–2939.

Behrendt, A. & Reichardt, J. (2000) Atmospheric temperature profiling in the presence of clouds with a pure rotational Raman lidar by use of an interference-filter-based polychromator. *Applied Optics*, 39, 1372–1378.

Behrendt, A., Wulfmeyer, V., Hammann, E., Muppa, S.K. & Pal, S. (2015) Profiles of second- to fourth-order moments of turbulent temperature fluctuations in the convective boundary layer: first measurements with rotational Raman lidar. *Atmospheric Chemistry and Physics*, 15, 5485–5500.

Bouillon, M., Safieddine, S., Hadji-Lazaro, J., Whitburn, S., Clarisse, L., Doutriaux-Boucher, M. et al. (2020) Ten-year assessment of IASI radiance and temperature. *Remote Sensing*, 12, 2393.

Brousseau, P., Seity, Y., Ricard, D. & Léger, J. (2016) Improvement of the forecast of convective activity from the AROME-France system: improvement of convective activity forecasts from AROME-France. *Quarterly Journal of the Royal Meteorological Society*, 142, 2231–2243.

Chazette, P., Clerbaux, C. & Mégie, G. (1998) Direct estimate of methane radiative forcing by use of nadir spectral radiances. *Applied Optics*, 37, 3113–3120.

Chazette, P., Flamant, C., Shang, X., Totems, J., Raut, J.-C., Doerenbecher, A. et al. (2016) A multi-instrument and multi-model assessment of atmospheric moisture variability over the western Mediterranean during HyMeX. *Quarterly Journal of the Royal Meteorological Society*, 142, 7–22.

Chazette, P., Marnas, F. & Totems, J. (2014) The mobile water vapor aerosol Raman LIdar and its implication in the framework of the HyMeX and ChArMEx programs: application to a dust transport process. *Atmospheric Measurement Techniques*, 7, 1629–1647.

Chazette, P., Totems, J., Ancellet, G., Pelon, J. & Sicard, M. (2016) Temporal consistency of lidar observations during aerosol transport events in the framework of the ChArMEx/ADRIMED campaign at Minorca in June 2013. *Atmospheric Chemistry and Physics*, 16, 2863–2875.

Chazette, P., Totems, J. & Shang, X. (2017) Atmospheric aerosol variability above the Paris area during the 2015 heat wave - comparison with the 2003 and 2006 heat waves. *Atmospheric Environment*, 170, 216–233.

Clerbaux, C., Boynard, A., Clarisse, L., George, M., Hadji-Lazaro, J., Herbin, H. et al. (2009) Monitoring of atmospheric composition using the thermal infrared IASI/MetOp sounder. *Atmospheric Chemistry and Physics*, 9, 6041–6054.

Clerbaux, C., Chazette, P., Hadji-Lazaro, J., Mégie, G., Müller, J.-F. & Clough, S.A. (1998) Remote sensing of CO, CH_4, and O_3 using a spaceborne nadir-viewing interferometer. *Journal of Geophysical Research-Atmospheres*, 103, 18999–19013.

Collard, A.D. & McNally, A.P. (2009) The assimilation of infrared atmospheric sounding interferometer radiances at ECMWF: Assimilation of IASI radiances at ECMWF. *Quarterly Journal of the Royal Meteorological Society*, 135, 1044–1058.

Cooney, J. (1972) Measurement of atmospheric temperature profiles by Raman backscatter. *Journal of Applied Meteorology (1962-1982)*, 11, 108–112.

Crevoisier, C., Clerbaux, C., Guidard, V., Phulpin, T., Armante, R., Barret, B. et al. (2014) Towards IASI-new generation (IASI-NG): impact of improved spectral resolution and radiometric noise on the retrieval of thermodynamic, chemistry and climate variables. *Atmospheric Measurement Techniques*, 7, 4367–4385.

Cuesta, J., Flamant, C., Gaetani, M., Knippertz, P., Fink, A.H., Chazette, P. et al. (2020) Three-dimensional pathways of dust over the Sahara during summer 2011 as revealed by new infrared atmospheric sounding interferometer observations. *Quarterly Journal of the Royal Meteorological Society*, 146, 2731–2755.

Déqué, M., Dreveton, C., Braun, A. & Cariolle, D. (1994) The ARPEGE/IFS atmosphere model: a contribution to the French community climate modelling. *Climate Dynamics*, 10, 249–266.

Deschênes, O. & Moretti, E. (2009) Extreme weather events, mortality, and migration. *The Review of Economics and Statistics*, 91, 659–681.

Di Girolamo, P., Cacciani, M., Summa, D., Scoccione, A., De Rosa, B., Behrendt, A. et al. (2017) Characterisation of boundary layer turbulent processes by the Raman lidar BASIL in the frame of $HD(CP)^2$ observational prototype experiment. *Atmospheric Chemistry and Physics*, 17, 745–767.

Di Girolamo, P., De Rosa, B., Flamant, C., Summa, D., Bousquet, O., Chazette, P. et al. (2020) Water vapor mixing ratio and temperature inter-comparison results in the framework of the hydrological cycle in the Mediterranean

experiment—special observation period 1. *Bulletin of Atmospheric Science and Technology*, 1, 113–153.

Di Girolamo, P., Marchese, R., Whiteman, D.N. & Demoz, B.B. (2004) Rotational Raman Lidar measurements of atmospheric temperature in the UV. *Geophysical Research Letters*, 31, 1106.

Dinoev, T., Simeonov, V., Arshinov, Y., Bobrovnikov, S., Ristori, P., Calpini, B. et al. (2013) Raman Lidar for meteorological observations, RALMO – part 1: instrument description. *Atmospheric Measurement Techniques*, 6, 1329–1346.

Domonkos, P. & Piotrowicz, K. (1998) Winter temperature characteristics in Central Europe. *International Journal of Climatology*, 18, 1405–1417.

Flamant, C., Chazette, P., Caumont, O., Di Girolamo, P., Behrendt, A., Sicard, M. et al. (2021) A network of water vapor Raman lidars for improving heavy precipitation forecasting in southern France – introducing the WaLiNeAs initiative. *Bulletin of Atmospheric Science and Technology*, 2, 10.

Frame, D.J., Rosier, S.M., Noy, I., Harrington, L.J., Carey-Smith, T., Sparrow, S.N. et al. (2020) Climate change attribution and the economic costs of extreme weather events: a study on damages from extreme rainfall and drought. *Climatic Change*, 162, 781–797.

Gerasimov, V.V. & Zuev, V.V. (2016) Analytical calibration functions for the pure rotational Raman lidar technique. *Optics Express*, 24, 5136–5151.

Hammann, E. & Behrendt, A. (2015) Parametrization of optimum filter passbands for rotational Raman temperature measurements. *Optics Express*, 23, 30767–30782.

Hammann, E., Behrendt, A., Le Mounier, F. & Wulfmeyer, V. (2015) Temperature profiling of the atmospheric boundary layer with rotational Raman lidar during the HD(CP)^2 observational prototype experiment. *Atmospheric Chemistry and Physics*, 15, 2867–2881.

Hauchecorne, A. & Chanin, M.-L. (1980) Density and temperature profiles obtained by lidar between 35 and 70 km. *Geophysical Research Letters*, 7, 565–568.

Hersbach, H., Bell, B., Berrisford, P., Hirahara, S., Horányi, A., Muñoz-Sabater, J. et al. (2020) The ERA5 global reanalysis. *Quarterly Journal of the Royal Meteorological Society*, 146, 1999–2049.

Johannsen, F., Ermida, S., Martins, J.p.A., Trigo, I.F., Nogueira, M. & Dutra, E. (2019) Cold bias of ERA5 summertime daily maximum land surface temperature over Iberian Peninsula. *Remote Sensing*, 11, 2570.

Klaes, K.D., Cohen, M., Buhler, Y., Schlüssel, P., Munro, R., Luntama, J.-P. et al. (2007) An introduction to the EUMETSAT polar system. *Bulletin of the American Meteorological Society*, 88, 1085–1096.

Kursinski, E.R., Hajj, G.A., Schofield, J.T., Linfield, R.P. & Hardy, K. R. (1997) Observing Earth's atmosphere with radio occultation measurements using the global positioning system. *Journal of Geophysical Research-Atmospheres*, 102, 23429–23465.

Kwon, E.-H., Sohn, B.J., Smith, W.L. & Li, J. (2012) Validating IASI temperature and moisture sounding retrievals over East Asia using radiosonde observations. *Journal of Atmospheric and Oceanic Technology*, 29, 1250–1262.

Lange, D., Behrendt, A. & Wulfmeyer, V. (2019) Compact operational tropospheric water vapor and temperature Raman Lidar with turbulence resolution. *Geophysical Research Letters*, 46, 14844–14853.

Lerner, J.A. (2002) Temperature and humidity retrieval from simulated infrared atmospheric sounding interferometer (IASI) measurements. *Journal of Geophysical Research*, 107, 4189.

Linnenluecke, M.K., Griffiths, A. & Winn, M. (2012) Extreme weather events and the critical importance of anticipatory adaptation and organizational resilience in responding to impacts. *Business Strategy and the Environment*, 21, 17–32.

Lowe, R., Ballester, J., Creswick, J., Robine, J.-M., Herrmann, F. & Rodó, X. (2015) Evaluating the performance of a climate-driven mortality model during heat waves and cold spells in Europe. *IJERPH*, 12, 1279–1294.

Martucci, G., Navas-Guzmán, F., Renaud, L., Romanens, G., Gamage, S.M., Hervo, M. et al. (2021) Validation of pure rotational Raman temperature data from the Raman Lidar for meteorological observations (RALMO) at Payerne. *Atmospheric Measurement Techniques*, 14, 1333–1353.

Mattis, I., Ansmann, A., Althausen, D., Jaenisch, V., Wandinger, U., Müller, D. et al. (2002) Relative-humidity profiling in the troposphere with a Raman lidar. *Applied Optics*, 41, 6451–6462.

Navas-Guzmán, F., Martucci, G., Collaud, C.M., Granados-Muñoz, M.J., Hervo, M., Sicard, M. et al. (2019) Characterization of aerosol hygroscopicity using Raman lidar measurements at the EARLINET station of Payerne. *Atmospheric Chemistry and Physics*, 19, 11651–11668.

Nedeljkovic, D., Hauchecorne, A. & Chanin, M. (1993) Rotational Raman lidar to measure the atmospheric temperature from the ground to 30 km. *IEEE Transactions on Geoscience and Remote Sensing*, 31, 90–101.

Noh, Y.-C., Sohn, B.-J., Kim, Y., Joo, S. & Bell, W. (2016) Evaluation of temperature and humidity profiles of unified model and ECMWF analyses using GRUAN radiosonde observations. *Atmosphere*, 7, 94.

Parmesan, C., Root, T.L. & Willig, M.R. (2000) Impacts of extreme weather and climate on terrestrial biota. *Bulletin of the American Meteorological Society*, 81, 443–450.

Penney, C.M., Peters, R.L.S. & Lapp, M. (1974) Absolute rotational Raman cross sections for N_2, O_2, and CO_2. *Journal of the Optical Society of America*, 64, 712–716.

Planchon, O., Quénol, H., Irimia, L. & Patriche, C. (2015) European cold wave during February 2012 and impacts in wine growing regions of Moldavia (Romania). *Theoretical and Applied Climatology*, 120, 469–478.

Pougatchev, N., August, T., Calbet, X., Hultberg, T., Oduleye, O., Schlüssel, P. et al. (2009) IASI temperature and water vapor retrievals – error assessment and validation. *Atmospheric Chemistry and Physics*, 9, 6453–6458.

Radlach, M., Behrendt, A. & Wulfmeyer, V. (2008) Scanning rotational Raman lidar at 355 nm for the measurement of tropospheric temperature fields. *Atmospheric Chemistry and Physics*, 8, 159–169.

Rodwell, M.J., Rowell, D.P. & Folland, C.K. (1999) Oceanic forcing of the wintertime North Atlantic oscillation and European climate. *Nature*, 398, 320–323.

Rosenzweig, C., Iglesius, A., Yang, X. B., Epstein, P., & Chivian, E. (2001). Climate change and extreme weather events - implications for food production, plant diseases, and pests. *NASA Publications*.

Royer, P., Chazette, P., Sartelet, K., Zhang, Q.J., Beekmann, M. & Raut, J.-C. (2011) Comparison of lidar-derived PM_{10} with regional modeling and ground-based observations in the frame of MEGAPOLI experiment. *Atmospheric Chemistry and Physics*, 11, 10705–10726.

Sandu, I., Beljaars, A., Bechtold, P., Mauritsen, T. & Balsamo, G. (2013) Why is it so difficult to represent stably stratified conditions in numerical weather prediction (NWP) models? *Journal of Advances in Modeling Earth Systems*, 5, 117–133.

Schlüssel, P., Hultberg, T.H., Phillips, p.L., August, T. & Calbet, X. (2005) The operational IASI level 2 processor. *Advances in Space Research*, 36, 982–988.

Sillmann, J. & Croci-Maspoli, M. (2009) Present and future atmospheric blocking and its impact on European mean and extreme climate. *Geophysical Research Letters*, 36. https://doi.org/10.1029/2009GL038259

Summa, D., Girolamo, p.D., Flamant, C., Rosa, B.D., Cacciani, M. & Stelitano, D. (2018) Water vapour intercomparison effort in the framework of the hydrological cycle in the mediterranean experiment – special observation period (hymex-sop1). *EPJ Web of Conferences*, 176, 08016.

Sutton, R.T. & Hodson, D.L.R. (2005) Atlantic Ocean forcing of north American and European summer climate. *Science*, 309, 115–118.

Tombette, M., Chazette, P., Sportisse, B. & Roustan, Y. (2008) Simulation of aerosol optical properties over Europe with a 3-D size-resolved aerosol model: comparisons with AERONET data. *Atmospheric Chemistry and Physics*, 8, 7115–7132.

Totems, J. & Chazette, P. (2016) Calibration of a water vapour Raman lidar with a kite-based humidity sensor. *Atmospheric Measurement Techniques*, 9, 1083–1094.

Totems, J., Chazette, P. & Baron, A. (2021) Mitigation of bias sources for atmospheric temperature and humidity in the mobile Raman weather and aerosol Lidar (WALI). *Atmospheric Measurement Techniques*, 14, 7525–7544.

Totems, J., Chazette, P. & Raut, J. (2019) Accuracy of current Arctic springtime water vapour estimates, assessed by Raman lidar. *Quarterly Journal of the Royal Meteorological Society*, 145, 1234–1249.

Vaughan, G., Wareing, D.P., Pepler, S.J., Thomas, L. & Mitev, V. (1993) Atmospheric temperature measurements made by rotational Raman scattering. *Applied Optics*, 32, 2758–2764.

Weitkamp, C. (Ed.). (2005) *Lidar: range-resolved optical remote sensing of the atmosphere*. New York: Springer-Verlag.

WMO. (2017). WMO OSCAR | List of all Requirements. Available at https://www.wmo-sat.info/oscar/requirements. Accessed March 2, 2021.

Wong, S., Fetzer, E.J., Schreier, M., Manipon, G., Fishbein, E.F., Kahn, B.H. et al. (2015) Cloud-induced uncertainties in AIRS and ECMWF temperature and specific humidity. *Journal of Geophysical Research-Atmospheres*, 120, 1880–1901.

Wulfmeyer, V., Bauer, H., Di Girolamo, P. & Serio, C. (2005) Comparison of active and passive water vapor remote sensing from space: an analysis based on the simulated performance of IASI and space borne differential absorption lidar. *Remote Sensing of Environment*, 95, 211–230.

APPENDIX A: EXTREME TEMPERATURE EVENTS IN FRANCE

The westerlies prevailing in the European mid-latitude troposphere, associated with the thermal inertia of the North Atlantic Ocean, make the western European climate mild in winter (Rodwell et al., 1999) and cool during summer (Sutton & Hodson, 2005). Occasionally, when the usual circulation regime is disturbed by atmospheric blocking (Sillmann & Croci-Maspoli, 2009), extremes events of temperature can be triggered. This appendix puts the episodes studied in the article into a more global climatological context of the occurrences of extreme temperature waves that have hit metropolitan France since the 1950s.

A.1. | Past cold waves in France

The event presented in this paper lasted 3 days (26 February–26 February) during the 2018 winter. To set this event in the wider context of CWs in France, an analysis of daily temperature data gathered by 41 Météo-France meteorological stations spatially distributed over continental France is performed. To extract the CWs in the 1950–2020 period from this dataset, the spatial average over the stations is computed and the result is only kept if 80% of the stations were operational at the same time. The dataset is reduced to the winter season (December–January–February) and the seasonal standard temperature T_{ST} is computed between 1981 and 2010 accordingly to the indicator defined by Météo-France. The results are presented in Figure A1: the selected CWs include at least a 3-day period with temperature below $T_{ST} - \sigma_{ST}$, where σ_{ST} is the standard deviation (STD) of the winter T_{ST}.

From this diagram, the historical cold winters that occurred in France since 1950 stand out clearly. The winter of 1963 was the coldest recorded in this period, but remarkable CWs occurred in 1954, 1956, 1985, 1987 and more recently in 2012. The CW of 2018, which is discussed in this paper, is not one of the strongest events, nonetheless it occurred extremely late in February. Such a late event is not frequent as only two CWs started after 20 February, in 1963 and 2018, and can have larger societal impacts in particular in agriculture (Planchon et al., 2015) or by triggering harmful particulate pollution episodes in urban areas (Baron et al., 2020).

FIGURE A1 Cold wave (CW) occurrence in France from 1950 to 2020. The maximum intensity (Y-axis) is the France-averaged temperature of the coldest day of each CW. The size of the disk indicates the severity of the CW, computed as a function of its duration, maximum intensity and mean temperature. The year n in white font centred in each disk relates to the winter of years $(n-1)/n$
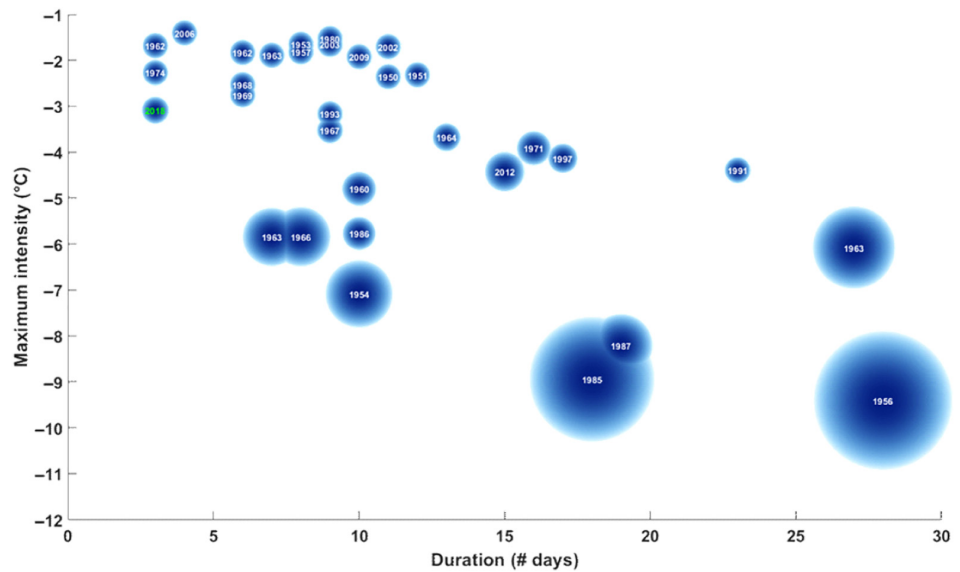

FIGURE A2 Heat wave (HW) occurrence in France from 1950 to 2020. The maximum intensity (Y-axis) is the France-averaged temperature of the warmest day of each HW. The size of the disk indicates the severity of the HW, computed as a function of its duration, maximum intensity and mean temperature. The corresponding year of each HW is noticed at the Centre of the disks in white font
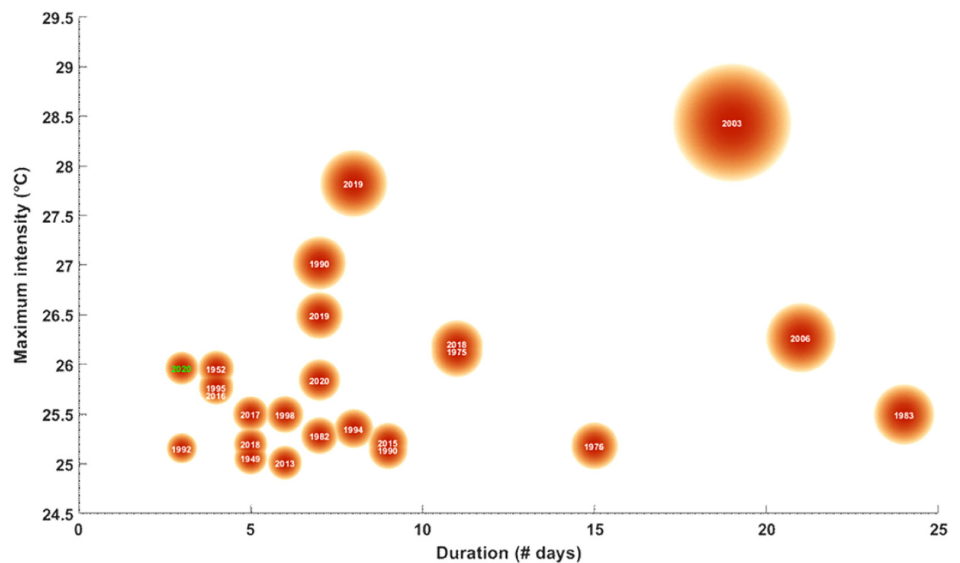
A.2. | Past heat waves in France

The summer event presented in this work is more a heat stroke than a heatwave. Felt in all Europe, it lasted 3 days from 31/07 to 02/08 in 2020. It marked the beginning of a warm period that lasted more than 2 weeks during which a second heat event occurred in mid-august. Just like for the winter case, Figure A2 represents the historic heatwaves that occurred in metropolitan France. The procedure is the same with this ready that June–July–August are used and the France-averaged temperature must overpass 25.3°C at least during 1 day of the period to be accounted for.

One can see the memorable heatwaves of 2003 and 2006 as part of the longest and/or the strongest events.

These events are known to be harmful to elderly and fragile people (Lowe et al., 2015), they also cause a great stress on the fauna and flora and trigger a variety of aerosol transport in the troposphere that can significantly modify the radiative budget (Chazette et al., 2017).

APPENDIX B: PRR SIGNAL PROCESSING AND TEMPERATURE CALIBRATION

In this appendix, we detail the signal processing specific to the WALI PRR lidar, the calibration process necessary to derive the temperature and we compute a theoretical error budget with a Monte Carlo simulation initialized with WALI's characteristics.
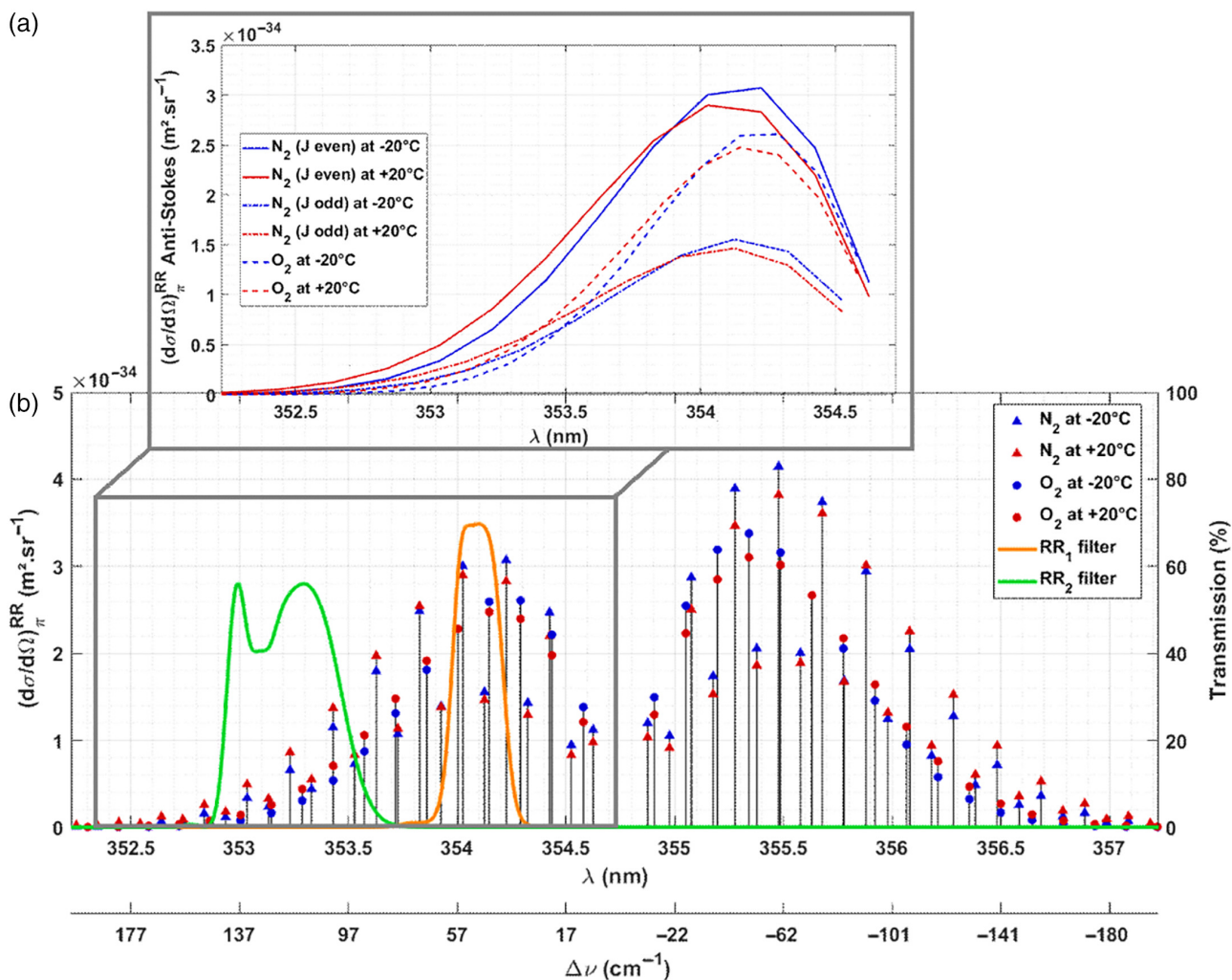
(a)

(b)

FIGURE B1 Rotational Raman spectrum of N_2 and O_2 with line intensities for two different temperatures ($-20°C$ and $+20°C$), (a). The RR1 (low rotational quantum number J value) and RR2 (high J value) filters are those used on the WALI lidar. They were measured using a spectroscope with a spectral resolution of 0.25 cm^{-1} and their transmissions are plotted in the right y-axis (b). A coefficient (the ratio of the O_2 mixing ratio vs. the N_2 mixing ratio ~ 0.27) is applied to the O_2 backscattering cross-sections (line intensities) to account for atmospheric mixing. By enlarging the anti-stokes part of the spectrum (top figure, b), the dissymmetry of the spectrum as a function of the temperature is highlighted: For high J values (left), the intensity increases with the temperature, for small values of J (right), the intensity of the lines decreases with the temperature

B.1. | PRR signal processing

The theory of temperature measurements using the pure rotational Raman technique is well described in the study by Behrendt (2006). Hereafter we propose a quick reminder of this technique. The asymmetric variation of the rotational Raman spectrum envelops the dinitrogen (N_2) and dioxygen (O_2) molecules of the air at the base of the PRR technique. From the expressions and parameter values found in the literature (e.g., Weitkamp, 2005), one can compute the rotational Raman spectrum of O_2 and N_2. Figure B1 displays this computation for two temperatures ($+20°C$ and $-20°C$). It shows the opposite variation

with temperature of the RR backscatter cross-section for low rotation quantum numbers (associated with the RR_1 filter) and for high rotation quantum numbers (RR_2 farther from the excitation wavelength of 354.725 nm).

In order to maximize the sensitivity with temperature, the ratio of the signals RR_2 on RR_1 is used. It is often named Q in the literature:

$$Q(z,T) = \frac{S_2^{RR_2}(\lambda_l, z, T)}{S_2^{RR_1}(\lambda_l, z, T)}. \tag{B1}$$

Since the filters cover more than one single RR line, this expression cannot be analytically inversed to retrieve the
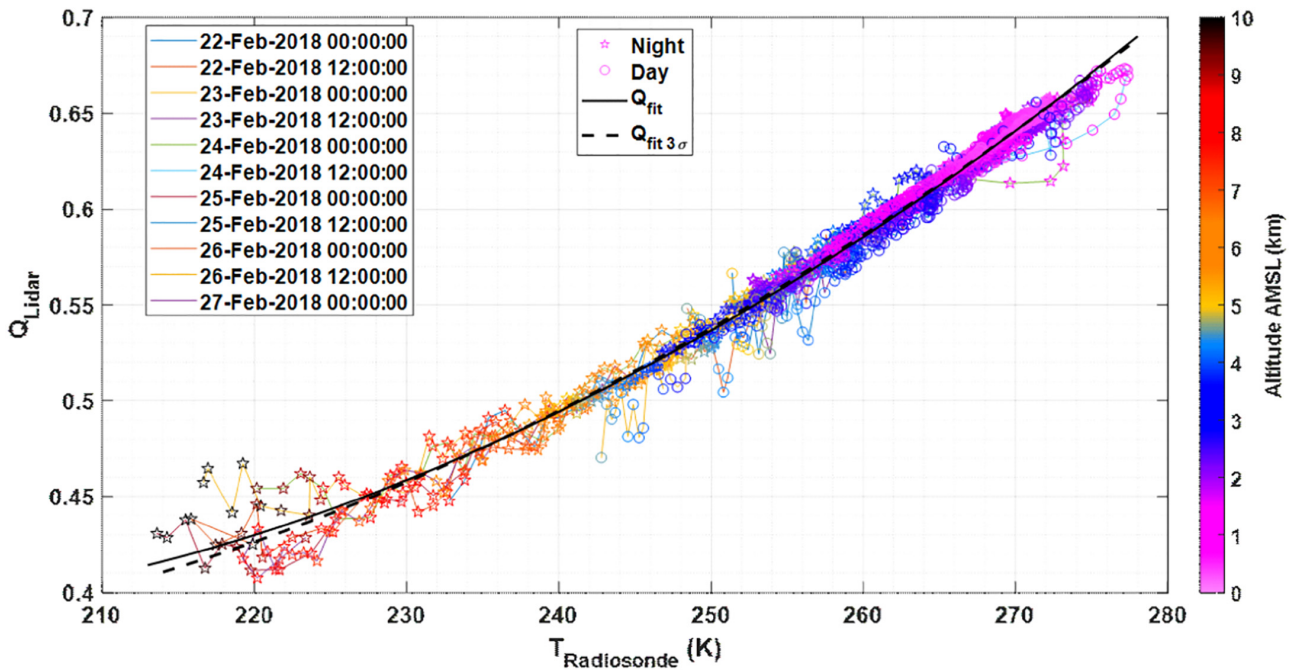
FIGURE B2 Calibration curve of the lidar for the February 2018 measurement sequence. The Q ratio is plotted against the coinciding radiosoundings. Coloured lines correspond to each radiosounding and a distinction is made for day and night with circle and star markers, respectively. The marker colour provides information on the altitude (coloured bar). The computed regression is plotted in solid black line. The dashed line represents the re-computation without data points further than 3 standard deviations from the original

temperature (Gerasimov & Zuev, 2016). The use of an approached calibration function is then necessary.

B.2. | Calibration

The more suitable calibration function has been the subject of several studies and can be chosen among a wide range of linear and non-linear functions (Gerasimov & Zuev, 2016). Here we choose to use a well-established non-linear function that expresses the Q ratio as the exponential of a second-order polynomial of the inverse of temperature (Behrendt, 2006):

$$
\begin{cases}
Q(T) = \exp\left(\dfrac{a}{T^2} + \dfrac{b}{T} + c\right) \\
T = \dfrac{-2a}{b + \sqrt{b^2 - 4a(c - \ln(Q))}}
\end{cases}
\tag{B2}
$$

Simulations conducted with this function allow to assess an intrinsic error lesser than 0.1°C for the filter used in the WALI.

In order to retrieve the calibration constants of the function in Equation (B2), exogenous measurements of

atmospheric temperature, preferably over the full range of expected temperatures, are necessary. The most convenient solution is to obtain profiles from radiosoundings launched close to the lidar site. In this study, the data used for the lidar calibration originates from the Trappes meteorological station of Météo-France (https://donneespubliques.meteofrance.fr). That station is located ~14 km westnorthwest of the lidar location. The fitted calibration curve used for the winter period in 2018 is displayed in Figure B2, where 11 radiosoundings from the entire measurement period are also plotted. Note that data points for which the lidar signal-to-noise ratio was found to be under 80 were rejected, so as not to bias the regression. The full temperature range is ~215 K to ~275 K, thanks to a sufficient signal-to-noise ratio (SNR) for night-time lidar data allowing to access altitudes up to 9 km AMSL with SNR > 80 (stars markers in Figure B2) where very cold temperatures can be encountered. The atmospheric temperature was measured down to −20°C around 2 km AMSL (purple markers) but above freezing at 3–4 km AMSL (up to ~3°C, blue markers).

Because of excess noise near the maximum range of the lidar or radiosondes sampling different air masses as they are carried away from the lidar location by the wind, outlying data points are still visible and additional
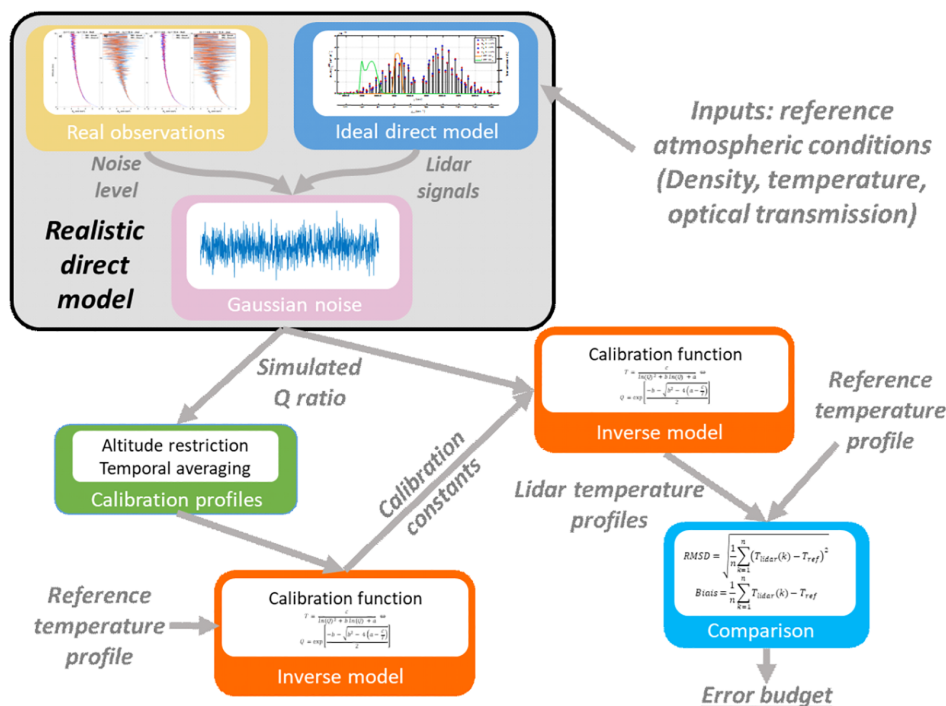
FIGURE B3 Block diagram of the direct-inverse model with Monte Carlo analysis. Random realistic lidar profiles are generated with noiseless simulated lidar profiles (upper blue block) with realistic level of noise (yellow block) and a Gaussian noise generator (pink block). Some of the profiles are picked up for calibration purposes using different restrictions in altitude (e.g., for day and night, green block). Calibration constants are then used to inverse the realistically simulated Q ratios (orange block) and the error budget is computed through the comparison with reference temperature used as an input (lower blue block)
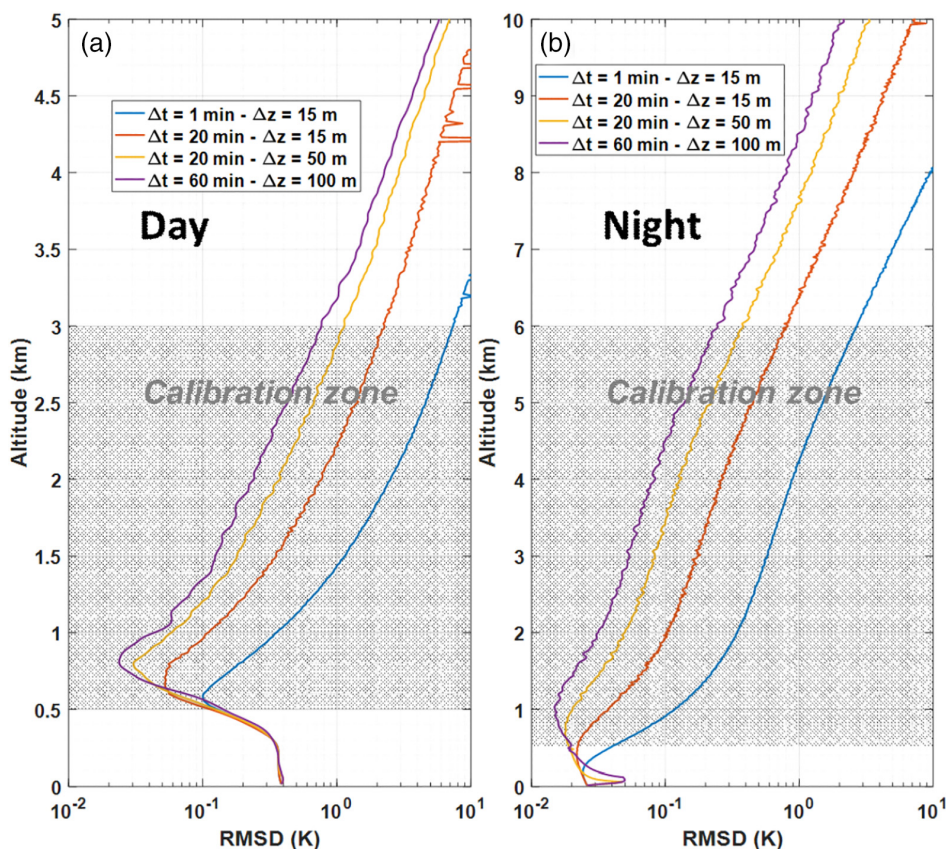

FIGURE B4 Root-mean-square deviation (RMSD) profiles of the WALI for daytime (a) or night-time (b) noise level (y-axis different). Four spatiotemporal resolutions are plotted. The pair $\Delta t = 1$ h and $\Delta z = 100$ m is used for calibration purposes. This calibration is performed using profiles parts restricted to 0.5–3 km for day (a) and 0.5–6 km for night (b), represented by shaded areas

rejection is required. The coefficients of Equation (3) are thus obtained by a regression computed only on points closer than 3 standard deviations from the original fit (dashed line in Figure B2). This latter fit contains the

calibration constants used to inverse the Q ratio into atmospheric temperature for the whole sequence of lidar measurements. Using a single radiosounding for calibration is expected to cause strong biases, in particular out of the

temperature range of this radiosonde profile. The RMSE is also expected to increase because of the lack of statistics to constrain the computation of calibration constants. To counteract this effect, all available radiosoundings are used to constrain the calibration coefficients computation. This results in a circulatory issue in the comparison between the lidar- and radiosounding-derived temperature profiles.

B.3. | Temperature error budget

The error budget of the lidar can be obtained both experimentally or through numerical simulations. Experimentally, the lidar temperature profiles are compared with concomitant exogenous measurements (typically radiosoundings). The indicators detailed in Appendix C, in particular the MB and the centred root-mean-square error, allow to assess the systematic and statistical errors inherent to lidar measurements as a function of the altitude range and the spatiotemporal resolutions used. Note that the mean bias calculated between lidar- and radiosounding-derived temperature profiles is not as relevant as if it had been calculated with a dedicated radiosonde dataset (independent from the calibration). Nevertheless, it allows to assess the accuracy of the calibration process. Better insights on the different bias sources and associated mitigation for Raman measurements (water vapour and temperature) made by WALI are detailed in Totems et al. (2021).

On the other hand, given the possibility for any temperature profile as input, to simulate lidar profiles using the theory presented in B1, one can numerically simulate realistic measurements, adding to ideal profiles a level of noise derived from previous measurements (Realistic direct model in Figure B3). These noise levels are obviously different for night-time or daytime measurements and a dichotomy must be made. Following a Monte Carlo method, random profiles are generated using Gaussian noise and some of them are picked up to be used to obtain the calibration constants. The restriction in altitude to prevent contamination by the overlap factor (low altitudes) and the noise level (higher in altitude) can be assessed in order to minimize the error and maximize the range of the lidar (green block in Figure B3). Moreover, different pairs of vertical and temporal resolutions are used to compute error profiles of temperature with this simulation.

The error budget calculated with the numerical simulations detailed above is summarized in Figure B4. Four pairs of vertical and temporal resolutions are used for calculations corresponding to daytime and night-time levels of noise. Calibration profiles used to constrain the calibration coefficients have a temporal resolution of 1 hr and a vertical resolution of 100 m. In practice, this time

is of the same order of magnitude than ascent duration of the balloon carrying the radiosonde used as a reference temperature profile. While the resolution used for calibration tends to flatten the noise, we still need to restrict the calibration zone below 3 and 6 km for day and night measurements. Furthermore, to prevent contamination from low altitude points that may be impacted by an imperfect correction of the overlap function, data are taken above 500 m for both cases.

The calibration constants are then used to inverse at least 200 random profiles and a comparison with the reference profile is used as input of the direct model. In Figure B4, we chose to represent the root-mean-square deviation which encompasses the systematic errors (bias) and the random errors (resulting from noise). One can see the different altitudes reached according to each pair of resolutions and for a temperature error lower than 1°C (WMO goal). These features fulfil the WMO requirements for temperature observations in the planetary boundary layer and the low troposphere. A compromise must be found between the desired maximum range and the finesse of the resolutions according to the processes to be studied.

One should notice that the increasing error near the surface is due to the altitude-restriction of lidar profiles at low altitudes to prevent overlap factor uncorrected residual to bias the calibration. This lack of constrain at these levels and given the non-linear nature of the calibration function, a bias appears near the surface. To best contain this bias, the overlap factor should be the lowest possible, allowing a greater calibration zone, especially critical for daytime measurements.

APPENDIX C: STATISTICAL PARAMETERS

Statistical parameters are commonly used for comparisons between models and observations (Tombette et al., 2008) or different instruments (Chazette, Flamant, et al., 2016). Here we choose to use the mean bias (MB), the Pearson correlation coefficient (COR), the root-mean-squared deviation (RMSD) and the centred root-mean-squared error (RMSE) to quantify the agreements and discrepancies between the different datasets. They are computed following the equations:

$$MB = \frac{1}{n}\sum_{k=1}^{n}(T_c(k) - T_{\text{Lidar}}(k)), \quad (C1)$$

$$COR = \frac{\frac{1}{n}\sum_{k=0}^{n}\left[\left(T_c(k) - \overline{T_c}\right) \times \left(T_{\text{Lidar}}(k) - \overline{T_{\text{Lidar}}}\right)\right]}{\sqrt{\sum_{k=1}^{n}\left(T_c(k) - \overline{T_c}\right)^2 \times \sum_{k=0}^{n}\left(T_{\text{Lidar}}(k) - \overline{T_{\text{Ldar}}}\right)^2}}, \quad (C2)$$

$$\text{RMSD} = \sqrt{\frac{1}{n}\sum\nolimits_{k=1}^{n}\left[T_c(k) - T_{\text{Lidar}}(k)\right]^2}, \qquad \text{(C3)}$$

$$\text{RMSE} = \sqrt{\frac{1}{n}\sum\nolimits_{k=1}^{n}\left[\left(T_c(k) - \overline{T_c}\right) - \left(T_{\text{Lidar}}(k) - \overline{T_{\text{Lidar}}}\right)\right]^2}, \qquad \text{(C4)}$$

where T_c is the temperature dataset to be compared with the coinciding lidar measurements. The MB allows to identify the systematic errors while the RMSE highlights the random ones. The RMSD compiles both information. The COR quantifies the linear relationship between two datasets. In our case, it depicts the degree of coherence of two datasets representing the same temperature time-height cross-section. For statistical profiles shown in this study, k runs over the available profiles at different time steps. For Table 1, the parameters are averaged in a second step over the sated altitude range.